INTERNATIONAL JOURNAL FOR NUMERICAL METHODS IN FLUIDS
Int. J. Numer. Meth. Fluids **30**: 675–711 (1999)

ON SPURIOUS BEHAVIOR OF CFD SIMULATIONS[1]

H.C. YEE[a,*], J.R. TORCZYNSKI[b], S.A. MORTON[c], M.R. VISBAL[c] AND
P.K. SWEBY[d,2]

[a] *NASA Ames Research Center, Moffett Field, CA 94035, USA*
[b] *Sandia National Laboratories, Albuquerque, NM 87185, USA*
[c] *CFD Research Branch, Wright Laboratory, Wright-Patterson AFB, OH 45433, USA*
[d] *Department of Mathematics, University of Reading, Whiteknights, Reading RG6 2AX, UK*

SUMMARY

Spurious behavior in underresolved grids and/or semi-implicit temporal discretizations for four computational fluid dynamics (CFD) simulations are studied. The numerical simulations consist of (a) a 1-D chemically relaxed non-equilibrium flow model, (b) the direct numerical simulation (DNS) of 2D incompressible flow over a backward facing step, (c) a loosely coupled approach for a 2D fluid–structure interaction, and (d) a 3D unsteady compressible flow simulation of vortex breakdown on delta wings. These examples were chosen based on their non-apparent spurious behaviors that were difficult to detect without extensive grid and/or temporal refinement studies and without some knowledge from dynamical systems theory. Studies revealed the various possible dangers of misinterpreting numerical simulation of realistic complex flows that are constrained by available computing power. In large scale computations, underresolved grids, semi-implicit procedures, loosely coupled implicit procedures, and insufficiently long-time integration in DNS are most often unavoidable. Consequently, care must be taken in both computation and in interpretation of the numerical data. The results presented confirm the important role that dynamical systems theory can play in the understanding of the non-linear behavior of numerical algorithms and in aiding the identification of the sources of numerical uncertainties in CFD. Copyright © 1999 John Wiley & Sons, Ltd.

KEY WORDS: computational fluid dynamics; numerical simulation; spurious behavior

1. INTRODUCTION

In a series of papers [1–8], the non-linear dynamics of finite discretizations for *constant time steps* and fixed or adaptive grid spacings was studied using tools from dynamical systems theory. The approach was to take continuum non-linear model ordinary differential equations (ODEs) and partial differential equations (PDEs) with known analytic solutions, discretize them according to various standard numerical methods, and apply techniques from discrete dynamical systems theory to analyze the non-linear behavior of the resulting non-linear difference equations. Particular attention was paid to the isolation of the different non-linear

---

* Correspondence to: NASA Ames Research Center, Moffett Field, CA 94035, USA.

[1] Invited paper AIAA-97-1969 for the *Proceedings of the 13th AIAA CFD Conference*, June 29–July 2, 1997, Snowmass, CO.

[2] Part of this work was performed as a visiting scientist at RIACS, NASA Ames Research Center.

Contract/grant sponsor: US Department of Energy; Contract/grant number: DE-ACO4-94AL85000
Contract/grant sponsor: Air Force Office of Scientific Research; Contract/grant number: Task 2307 AW

CCC 0271–2091/99/140675–37$17.50

Received 5 May 1997
Revised 21 June 1998

behavior and spurious dynamics due to some of the numerical uncertainties that were observed in practical computational fluid dynamics (CFD) computations. Here, spurious solutions refer to numerical artifacts or physically irrelevant solutions. They are true solutions of the resulting non-linear difference equations but are not solutions of the governing equations. The numerical schemes considered for these non-linear model ODEs and PDEs were selected to illustrate the following different non-linear behavior of numerical methods:

- Occurrence of stable and unstable spurious asymptotes *above* the linearized stability limit of the scheme (for constant time steps) [1–4].
- Occurrence of stable and unstable spurious steady states *below* the linearized stability limit of the scheme (for constant time steps) [1–4].
- *Stabilization* of unstable steady states by implicit and semi-implicit methods [2–4].
- Interplay of initial data and time steps on the occurrence of spurious asymptotes [2–4].
- Interference with the dynamics of the underlying implicit scheme by procedures in solving the non-linear algebraic equations (resulting from implicit discretization of the continuum equations) [2,4].
- Dynamics of the linearized implicit Euler scheme solving the time-dependent equations versus Newton's method solving the steady equation [3].
- Spurious dynamics independently introduced by spatial and time discretizations [5,6].
- Convergence problems and spurious behavior of high resolution shock capturing methods [4].
- Numerically induced and suppressed chaos, and numerically induced chaotic transients [2,9].
- Spurious dynamics generated by grid adaptations [2,4].

For time-accurate computations, variable time steps based on local error control [10,11] or adaptive time steps and grid spacings based on error control [12–14] are more suitable than constant time steps and grid spacings. With the exception of finite element methods, variable time steps based on local error control or adaptive methods are not at a point where they are either efficient or practical for CFD computations. The rationale for the study of the dynamics of constant step sizes is that the majority of time-accurate CFD computations are still based on constant time steps and grid spacings that satisfy a given CFL condition.

The type of study performed in References [1–8,15] is often viewed in the CFD community as of academic interest, and the results found are often dismissed as irrelevant to practical CFD computations. The general consensus is that except for special situations, an analysis similar to that in References [1–8], is not possible for more complicated models. Nevertheless, Yee and Sweby [9,16] believe phenomena observed in simple non-linear model problems can serve as guidelines in practical computations, akin to the use of the CFL condition for the selection of time steps for highly coupled non-linear problems. They believe that the knowledge gained from non-linear behavior of numerical schemes using dynamical systems theory can help to explain and minimize numerical uncertainties in CFD. This stems from the fact that highly non-linear and/or stiff problems do not always lend themselves to the traditional numerical analysis and standard CFD practices. A knowledge of 'dynamical numerical analysis' is necessary to pinpoint the source of numerical uncertainties. To support their beliefs, Yee and Sweby [9,16] took the initiative to illustrate this connection. To correlate the knowledge gained from the aforementioned studies with practical computations, Yee and Sweby [16] identified some examples in time marching to the steady state CFD computations that exhibit behavior similar to that of the simple model case. They gave an overview [9] of the subject with some unsteady CFD examples. These later studies exemplify the importance of the knowledge gained in the non-linear behavior of numerical schemes if the physics of the problem under study is not well-understood and numerical simulations are the only viable means of solutions.

The present study continues the same line of research but concentrates on spurious behavior in underresolved grids and/or semi-implicit time discretizations for four realistic time-accurate CFD simulations. The numerical simulations consist of (a) a 1D chemically relaxed non-equilibrium flow model, (b) the direct numerical simulation (DNS) of 2D incompressible flow over a backward facing step, (c) a loosely coupled approach for a 2D fluid–structure interaction, and (d) a 3D unsteady compressible flow simulation of vortex breakdown on delta wings. These examples were chosen based on their non-apparent spurious behavior that is difficult to detect without extensive grid and/or temporal refinement studies and some knowledge from dynamical systems theory. The main purpose of the present study is to illustrate that inaccuracy associated with underresolved grids (e.g. disappearance of the fine details of the flow due to large numerical dissipation and/or low order of the scheme) and linear instability associated with time discretizations are easier to detect than spurious numerical solutions.

As shown in subsequent sections, the allowable upstream initial inputs strongly depend on the grid spacing for the 1D chemically relaxed non-equilibrium flow model. There is a drastic reduction in the basins of the initial upstream inputs with a slight increase in grid spacing. The semi-implicit time-like discretizations behave in a manner similar to standard explicit Runge–Kutta methods except the allowable upstream initial inputs are slightly less sensitive to the grid spacing. Spurious time periodic solutions exist for grid spacings that are near the stability limit. Long-time transients or chaotic-like transients followed by divergent or spurious time periodic solutions were observed for the backward-facing step simulations using a spectral element method if sufficiently long-time integrations were performed. Insufficiently long time integration in conjunction with underresolved grids can lead to the erroneous conclusion of chaotic flow. Time asymptotic numerical solutions are sensitive to initial conditions. Spurious time periodic solutions and numerically induced chaotic-like behavior were observed for a 2D fluid–structure interaction using a loosely coupled (time lag) implicit temporal procedure of solving the fluid and structure equations. The spurious behavior ceased to exist if a fully coupled procedure is used. Non-unique numerical solutions, some of which are spurious, were observed as a function of initial angles of attack in vortex breakdown on delta wing simulations using a fully implicit procedure. A grid refinement study confirmed that the non-unique solutions are numerical artifacts and are independent of the studied initial angles of attack.

The present study serves to point out the various possible dangers of misinterpreting numerical simulations of realistic complex flows that are constrained by available computing power. In large scale computations, underresolved grids, semi-implicit procedures, loosely coupled implicit procedures, and insufficiently long time integration in DNS are most often unavoidable. Consequently, care must be taken in both computation and in interpretation of the numerical data. A good knowledge of the non-linear dynamical behavior of numerical schemes is shown to be very useful. Details of the four CFD simulations will be presented in the next four sections. An analysis similar to that in References [2–4] is only possible for the 1D chemically relaxed non-equilibrium flow model. Note that the background material presented in Section 2.1 on the interplay of initial data and time steps on the occurrence of spurious numerical solutions is relevant for Sections 2–4.

2. A 1D CHEMICALLY RELAXED NON-EQUILIBRIUM MODEL

Before discussing the numerical simulations of the 1D chemically relaxed non-equilibrium flow model, relevant background on the interplay of initial data and time steps on the occurrence of spurious asymptotes is presented.

2.1. Strong dependence on initial data

The global asymptotic non-linear behavior and bifurcation phenomena for the explicit Euler method, five different multistage Runge–Kutta methods (modified Euler, improved Euler, Heun, Kutta and fourth-order methods), two- and three-step predictor–corrector methods, Adams–Bashforth method, a semi-implicit method, and four implicit linear multistep methods (LMMs) (implicit Euler, trapezoidal, three-point backward differentiation (BDF) and mid-point implicit methods) with four ways for solving the non-linear algebraic equations are compared for different non-linear model ODEs in References [1–4]. Their emphasis is on the interplay of initial data and time steps on the occurrence of spurious asymptotic numerical solutions. The four ways for solving the non-linear algebraic equations considered are the non-iterative linearized form, simple iteration, Newton and modified Newton methods.

One of the key concepts in understanding the interplay of initial data and time steps on the occurrence of spurious asymptotes is *Basins of Attraction*. The basin of attraction of an asymptote (for the differential equations (DEs) or their discretized counterparts) is a set of all initial data asymptotically approaching that asymptote. Here, the discretized counterparts refer to the finite difference equations resulting from finite discretizations of the DEs. In other words, a basin of attraction tells which initial data lead to which asymptotes. For each asymptote of the DE and the underlying difference equation, the terms 'exact' basin of attraction and 'numerical' basin of attraction refer to the basin of attraction of the DE and basin of attraction of the underlying discretized counterpart respectively. For a constant time step, spurious asymptotic numerical solutions, if they exist, occupy their own numerical basins of attraction. The sizes of these basins of attraction varies from one time step to another, and consequently interfere with the sizes of the numerical basins of attraction of the true steady states.

In [2–6], the authors showed how numerical basins of attraction can help in gaining a better understanding of the global asymptotic behavior of numerical solutions for non-linear DEs. In particular, they showed how in the presence of spurious asymptotes, the basins of the true stable steady states can be segmented by the basins of the spurious stable and unstable asymptotes. One major consequence of this phenomenon, which is *not commonly known*, is that this spurious behavior can result in a dramatic distortion and, in most cases, a dramatic shrinkage and segmentation of the basin of attraction of the true solution for finite time steps. Such distortion, shrinkage and segmentation of the numerical basins of attraction will occur regardless of the stability of the spurious asymptotes. In other words, the size of the domain of initial data approaching the underlying asymptotes changes with the time step even when one operates with time steps that are below the linearized stability limit. Studies showed that all of the four implicit LMMs exhibit a drastic distortion but less shrinkage of the basin of attraction of the true solution than explicit methods. As is the case for standard explicit methods, but in some cases with smaller Δt, the implicit LMMs exhibit enlargement of the basins of attraction of the true solution. Such enlargement occurs when Δt is small or in the vicinity of the stability limit of standard explicit method counterparts. The semi-implicit method exhibits behavior that combines those of the explicit and implicit methods. Spurious behavior of a different semi-implicit method applied to a convection reaction equation can be found in [5,6]. An important implication of the basin of attraction study is that associated with a static initial data, stable spurious solutions, if they exist, are also very likely to be *stable under static initial data perturbations*.

There are a variety of semi-implicit procedures for a chosen implicit scheme. For systems of highly coupled compressible and incompressible Euler and Navier–Stokes equations with or without source terms, an exhaustive list is beyond the scope of the present paper. This paper examines the spurious behavior of three commonly used semi-implicit procedures in CFD simulations. In this section, a semi-implicit form of the implicit Euler and trapezoidal methods are studied. In Section 3, a mixed explicit and implicit form of a spectral element method is discussed. In Section 4, a time lag semi-implicit form for a fluid–structure interaction is discussed.

2.2. Spurious behavior of a 1D reaction model

This section discusses the analysis of numerical basins of attraction for the simulation of a 1D chemically relaxed non-equilibrium flow model for a (N_2, N) mixture. Sweby *et al.* [17] and Section 4.1 of [9] studied the spurious behavior of this model for six different explicit Runge–Kutta methods. Here the authors will look at the semi-implicit form of the implicit Euler and trapezoidal formula and compare the result with the explicit methods. This type of flow is encountered in various physical situations, such as shock tube experiments (the mixture behind the shock being in a highly non-equilibrium state) or a high enthalpy hypersonic wind tunnel. Under these assumptions, the model can be expressed as a single ODE,

$$\frac{\mathrm{d}z}{\mathrm{d}x} = S(\rho, T, z), \tag{2.1}$$

where z is the mass fraction of the N_2 species, ρ is the density of the mixture and T is the temperature. There are two algebraic equations for ρ and T. This system is stiff and highly non-linear.

The derivation of the model is as follows. The 1D steady Euler equations for a reacting (N_2, N) mixture are

$$\frac{\mathrm{d}}{\mathrm{d}x}(\rho_{N_2} u) = \dot{w}_{N_2}, \tag{2.2a}$$

$$\frac{\mathrm{d}}{\mathrm{d}x}(\rho u) = 0, \tag{2.2b}$$

$$\frac{\mathrm{d}}{\mathrm{d}x}(\rho u^2 + p) = 0, \tag{2.2c}$$

$$\frac{\mathrm{d}}{\mathrm{d}x}[u(E + p)] = 0, \tag{2.2d}$$

where (2.2a) is the balance equation for the N_2 species and $\dot{w}_{N_2}$ is the production rate of the N_2 species with density ρ_{N_2}. The variables ρ, u, E and p are density, velocity, total internal energy per unit volume and pressure respectively.

The production rate $\dot{w}_{N_2}$ of species N_2 is the sum of the production rates for the two reactions

$$N_2 + N_2 \rightleftharpoons 2N + N_2, \tag{2.3a}$$

$$N_2 + N \rightleftharpoons 2N + N \tag{2.3b}$$

and is computed using Park's model [18] that has been used extensively for hypersonic computations. See [19] for some discussion. These reaction rates involve an equilibrium constant, K_{eq} (see below), which is determined by a polynomial fitting to experimental data, and as such is only valid for a certain range of temperatures. In particular, a cut-off value has to be introduced for low temperatures, a typical choice being $T_{min} = 1000$ K [20].

The systems (2.2) and (2.3) must be closed by a thermodynamic representation of the mixture. Here, a simple model, with no vibrational effects, has been chosen. The details have been omitted for brevity.

Equations (2.2b)–(2.2d) simply integrate to give

$$\rho u = q_\infty, \tag{2.4a}$$

$$\rho u^2 + p = P_\infty, \tag{2.4b}$$

$$H = \frac{E+p}{\rho} = H_\infty, \tag{2.4c}$$

where H is the total enthalpy and q_∞, P_∞ and H_∞ are all constants. Finally, denoting the mass fraction of the N_2 species by

$$z = \frac{\rho_{N_2}}{\rho}, \tag{2.5}$$

and using Park's reaction rate model and the thermodynamic closure, (2.1) can be written as

$$\frac{dz}{dx} = S(\rho, T, z) = \frac{1}{M_1 q_\infty} \rho^2 T^B \exp\left(-\frac{\theta}{T}\right)$$
$$\times [\alpha A_1 z(1-z)^2 - A_1 z^2 + 2\alpha A_2 (1-z)^3 - 2A_2 z(1-z)], \tag{2.6a}$$

where

$$\alpha = \frac{4\rho}{M_1 K_{eq}}, \quad K_{eq} = 10^6 \exp[c_1 + c_2 Z + c_3 Z^2 + c_4 Z^3 + c_5 Z^4], \quad Z = \frac{10^4}{T}. \tag{2.6b}$$

The density ρ is obtained from

$$q_\infty^2 (8-2z)\left(\frac{1}{\rho}\right)^2 - (10-3z)P_\infty \left(\frac{1}{\rho}\right) + 2(2-z)[H_\infty - (1-z)e_2^0] = 0 \tag{2.6c}$$

and the temperature T from

$$T = \frac{M_1 p}{R(2-z)\rho} \tag{2.6d}$$

and the pressure from

$$p = P_\infty - \frac{q_\infty^2}{\rho}. \tag{2.6e}$$

The model uses the constants

$$\begin{bmatrix} c_1 = 3.898 \\ c_2 = -12.611 \\ c_3 = 0.683 \\ c_4 = -0.118 \\ c_5 = 0.006 \\ M_1 = 28 \times 10^3 \end{bmatrix} \qquad \begin{bmatrix} A_1 = 3.7 \times 10^{15} \\ A_2 = 1.11 \times 10^{16} \\ B = -1.6 \\ \theta = 1.132 \times 10^5 \\ e_2^0 = 3.355 \times 10^7 \\ R = 8.3143 \end{bmatrix}.$$

The input parameters q_∞, P_∞ and H_∞ are set equal to 0.0561, 158 000 and 27 400 000 respectively. A limitation of the model is $T > T_{\min} = 1000$ K. The acceptable root of (2.6c) is taken to be real and positive. In addition, solutions are non-physical if $z \notin [0, 1]$, if $p < 0$ or if ρ is complex.

In the integration of (2.1), the spatial variable z acts as a time-like variable. The asymptotic state is the equilibrium state given by $S(\rho, T, z) = 0$. Equation (2.6a) was integrated using the Euler, modified Euler (R–K 2) improved Euler (R–K 2), Heun (R–K 3), Kutta (R–K 3), fourth-order Runge–Kutta (R–K 4) schemes and a semi-implicit version of the implicit Euler and trapezoidal methods.

There are two strategies possible when implementing these schemes. One is to freeze the values of ρ and T at the beginning of each step when calculating $S(\rho, T, z)$ at the intermediate stages. The other is to update the values at each evaluation of the function S. The results presented here employ the latter strategy since this is the more proper implementation; however, it is interesting to note (see below) that results obtained by freezing ρ and T for intermediate calculations exhibit a slightly richer dynamical structure. Due to the complexity of the equation and the coupling of the unknowns, the implicit method was implemented by treating the z variable implicitly and the rest of the unknowns explicitly.

In each case, the computations were performed for a range of initial z and integration steps Δx. For each fixed Δx and each initial datum, the discretized equations were pre-iterated 1000 steps before a full bifurcation diagram (of the asymptotic states) together with basins of attraction were produced. The pre-iterations are necessary in order for the solutions to settle to their asymptotic values. To obtain a bifurcation diagram with numerical basins of attraction superimposed, the pre-selected domain of initial data and the pre-selected range of the Δx parameter are divided into 256 or 512 equal increments. We keep track of where each initial datum asymptotically approaches, and color code each basin according to the individual asymptotes. Figures 1 and 2 show the results obtained from these computations. Due to the fact that for each Δx, only two distinct basins of attraction are present for all of the computations, only the grey scale version of these plots are shown. In all of these plots, the shaded region denotes the basin of attraction in which combinations of 'initial' upstream input z values and step size Δx converge to the stable asymptotes of the discretized equations, depicted by the solid black line or black dots. The unshaded regions indicate regions of upstream initial input where the combinations of upstream input z and Δx do not converge or converge to a non-physical solution of the problem (see condition below (2.6e)). As can be seen in all cases, there is a drastic reduction in the basins of attraction with just a slight increase in the grid spacing. (The axis scale is 10^{-5}!) Note that the allowable upstream initial input (exact basin of attraction) for the governing equation (2.1) is $0 \leq z \leq 1$.

2.2.1. Explicit Runge–Kutta methods. The explicit Euler scheme (Figure 1(a)) obtains the correct equilibrium state up to its linearized stability limit, where there is a very small region of period two spurious solutions before it diverges. Similar behavior is observed for the improved Euler (Figure 1(c)) and Kutta (Figure 1(e)) schemes, the latter also exhibiting a much more constricted basin of attraction for any given Δx. The Heun scheme (Figure 1(d)) exhibits a distinct region where stable spurious periodic solutions occurred just above the linearized stability limit.

As is typical with the modified Euler scheme (Figure 1(b)), a transcritical bifurcation occurs at its stability limit which leads to a spurious (Δx dependent) solution near the stability limit. Note also the solid line at about $z = 0.25$ on the plot, outside of the shaded region. This appears to be an unstable feature picked up by this method of asymptotic equilibrium state

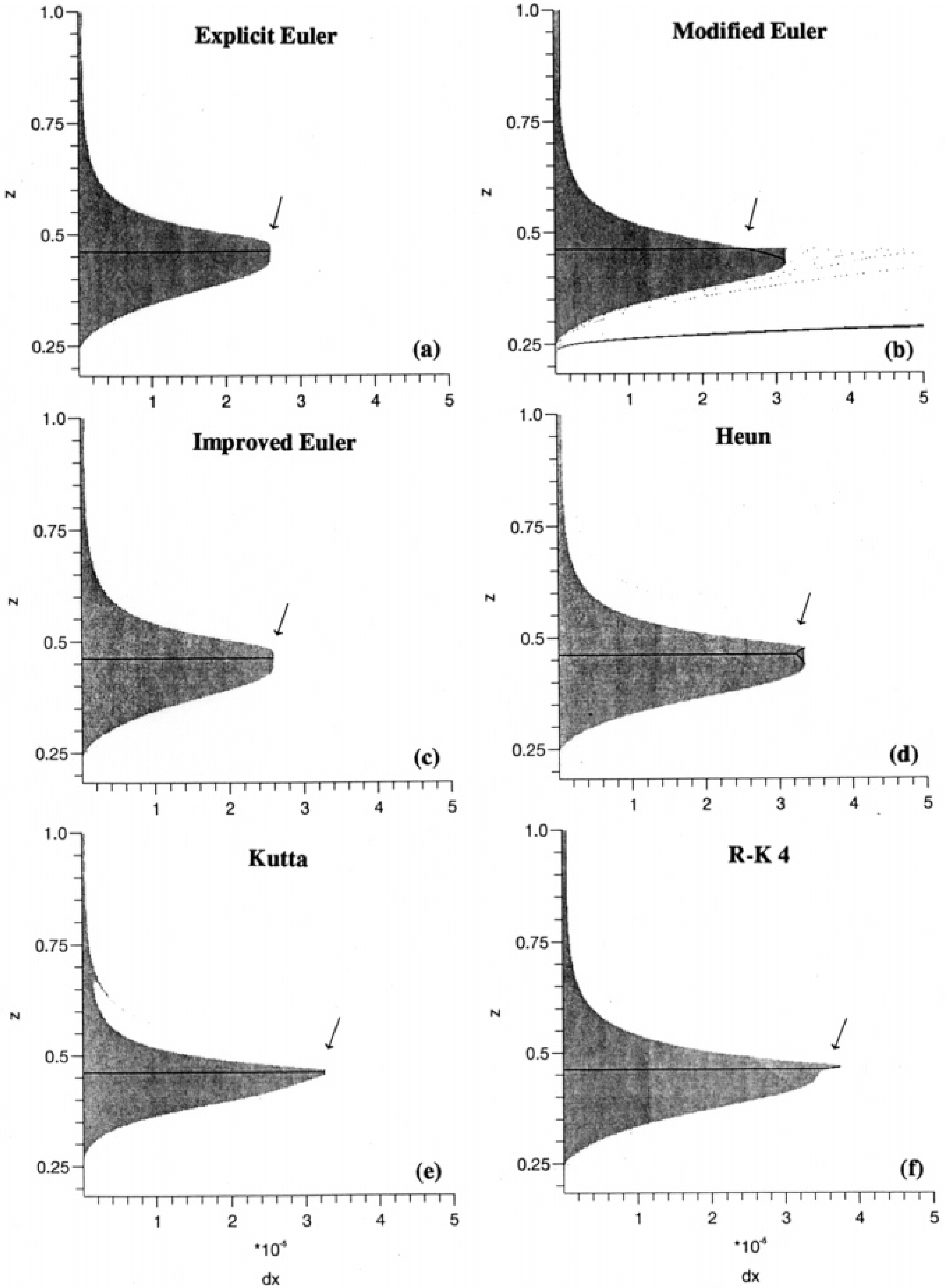

Figure 1. Bifurcation diagrams and basins of attractions of asymptotes of six explicit methods for the two-species reacting flow (arrows indicate the linearized stability limits).

detection (comparison of initial data with the 1000th iterate) and is unlikely to arise in practical calculations unless the initial data are on this curve. The R–K 4 scheme (Figure 1(f)) also exhibits a transcritical bifurcation at the linearized stability limit; however, this is discernible more by the sudden narrowing of the basin of attraction since the spurious asymptotic state varies only slightly with Δx.

If the values of ρ and T are frozen for intermediate calculations, the dynamics are somewhat modified. All schemes with the exception of explicit Euler have a slightly larger basin of attraction for values of Δx within the stability limit and *all* schemes have period two behavior at the stability limit, there being no transcritical bifurcations for any of the schemes. The

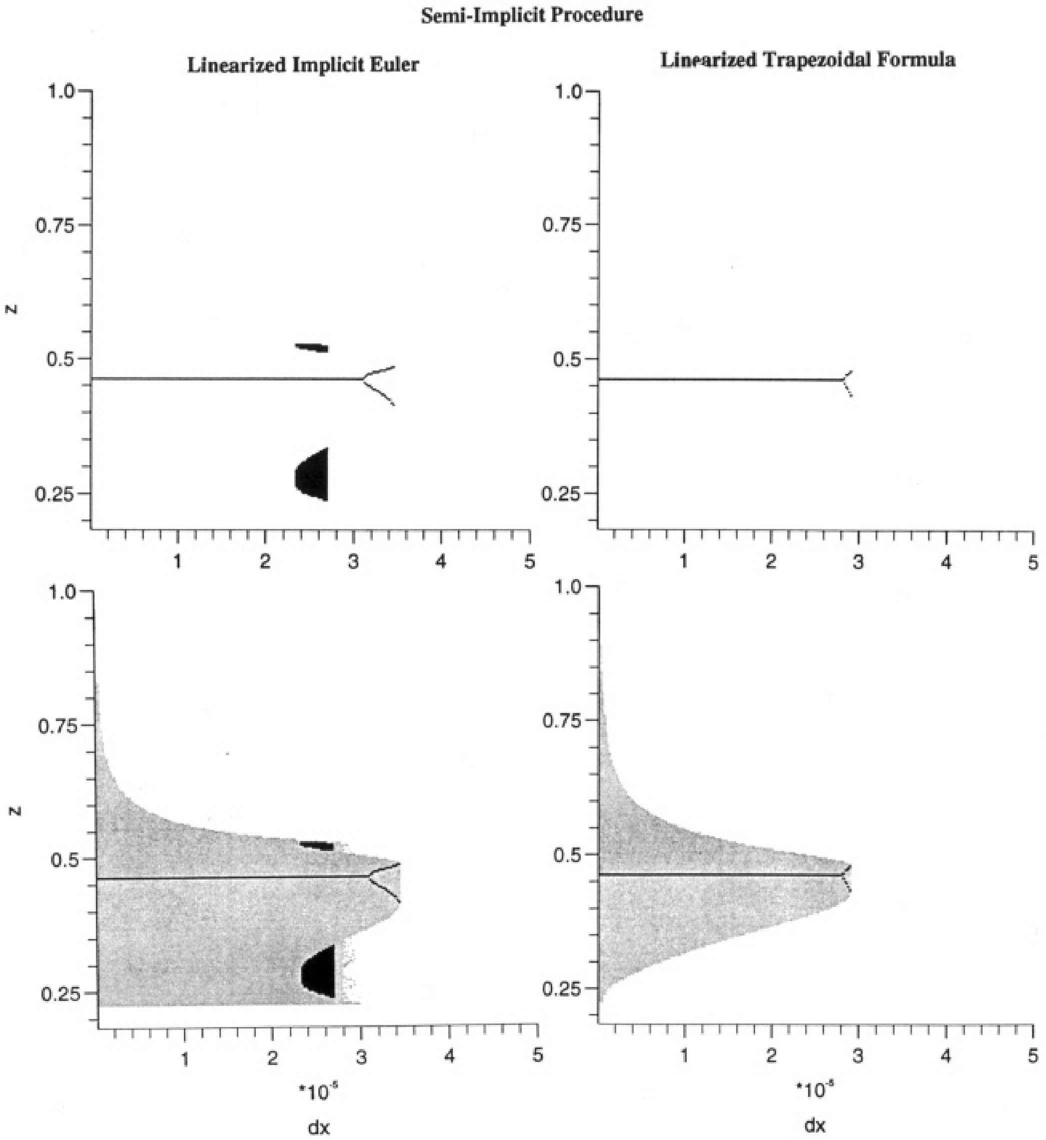

Figure 2. Bifurcation diagrams (top) and bifurcation diagrams with basins of attraction superimposed (bottom) of asymptotes of semi-implicit methods for the two-species reacting flow.

modified Euler scheme also has embedded period doubling and chaotic behavior below the linearized stability limit. For the classification of bifurcation points and their effects on the existence of spurious asymptotic numerical solutions, see [1,9].

2.2.2. Semi-implicit methods. Due to the complexity of the equation and the coupling of the unknowns, the implicit method was implemented by treating the z variable implicitly and the rest of the unknowns explicitly. Only the linearized version (non-iterative) of the implicit Euler and trapezoidal formula is considered. To aid the discussions, bifurcation diagrams and the bifurcation diagrams with the basins of attraction superimposed on the same plot are shown in Figure 2 using this semi-implicit approach. Both methods behave in a manner similar to their explicit counterparts, except that the reduction in the basins of attraction (as Δx increases) is considerably less than the explicit Runge–Kutta methods for the implicit Euler but only slightly larger for the trapezoidal method. In addition, the semi-implicit Euler approach exhibits a richer dynamical structure than the rest of the methods studied. Besides a definite region where period two spurious solutions bifurcate from the true branch of the steady state solutions near $\Delta x = 3.1 \times 10^{-5}$, spurious periodic solutions up to period 480 occur for smaller Δx (see the two dark regions for $2.34 \times 10^{-5} \leq \Delta x \leq 2.7 \times 10^{-5}$). These spurious asymptotes appear to be chaotic-like. In other words, it is possible that for the same grid spacing but different initial input, the numerical solution converges to two different solutions. For $2.34 \times 10^{-5} \leq \Delta x \leq 2.7 \times 10^{-5}$, one of the numerical solutions is spurious (initial data reside on the shaded region or on the two darker regions). For $\Delta x > 3.1 \times 10^{-5}$, all of the numerical solutions are spurious.

The above computations illustrate the sensitivity of the allowable upstream initial inputs to the slight increase in the grid spacing. In other words, with a slight increase in the grid spacing, the allowable upstream initial inputs quickly become ‘numerically unphysical’. Although the dynamical behavior of the studied schemes is perhaps not as rich as in some of the simple examples discussed in [1–6], spurious features can still occur in practical calculations and so care must be taken in both computation and in interpretation.

3. DNS OF 2D INCOMPRESSIBLE FLOW OVER A BACKWARD-FACING STEP

In addition to the inherent chaotic and chaotic transient behavior in some physical systems, numerics can independently introduce and suppress chaos as well as chaotic transients. Section 5.1 of [16] shows a practical example of a numerically induced chaotic transient near the onset of turbulence in a direct numerical simulation of a 3D channel flow studied by Keefe [21]. Loosely speaking, a chaotic transient behaves like a chaotic solution [22]. A chaotic transient can occur in a continuum or a discrete dynamical system. One of the major characteristics of a numerically induced chaotic transient is that if one does not integrate the discretized equations long enough, the numerical solution has all the characteristics of a chaotic solution. The required number of integration steps might be extremely large before the numerical solution can get out of the chaotic transient mode. In addition, standard numerical methods, depending on the initial data, usually experience drastic reductions in step size and convergence rate near a bifurcation point (in this case the transition point) in addition to the bifurcation points due solely to the discretized parameters. See [2,3,16] for a discussion. Consequently, the possible numerically induced chaotic transient is especially worrisome in direct numerical simulations of transition from laminar to turbulent flows. Except for special situations, it is impossible to compute the exact transition point by mere DNS of the

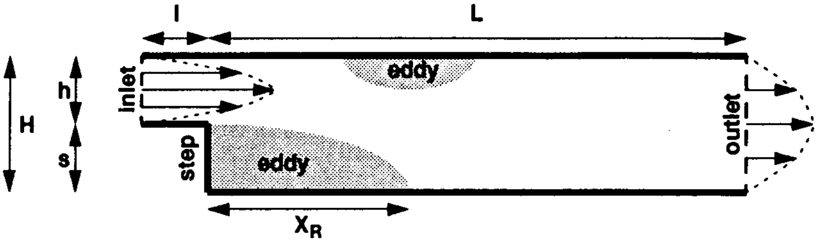

Figure 3. Schematic diagram of flow over a backward-facing step.

Navier–Stokes equations. Even away from the transition point, this type of numerical simulation is already very CPU intensive and the convergence rate is usually rather slow. Due to the limited computer resources, the numerical simulation can result in chaotic transients indistinguishable from sustained turbulence, yielding a spurious picture of the flow for a given Reynolds number. Consequently, it casts some doubt on the reliability of numerically predicted transition points and chaotic flows. It also influences the true connection between chaos and turbulence. See also [23]. The present section and Sections 4 and 5 make use of this knowledge from continuum and discrete dynamical systems theory to identify some of the aforementioned numerical uncertainties.

3.1. Background and objective

The 2D incompressible flow over a backward-facing step has been addressed by many authors using a wide variety of numerical methods. Figure 3 shows the flow geometry. Fluid with constant density ρ and viscosity μ enters the upstream channel of height h with a prescribed velocity profile (usually parabolic). After traveling a distance l, the fluid passes over a backward-facing step of height s and enters the downstream channel of height $H = h + s$. After traveling a distance L downstream of the step, the fluid exits the region of interest. For Reynolds numbers considered here, the flow separates at the corner and forms a recirculating region of length X_R behind the step. Additional recirculating regions form on the upper, and subsequently, the lower walls of the downstream channel as the Reynolds number is increased.

Results of sustained unsteady flow from various numerical simulations have been reported for Reynolds numbers (*Re*) ranging from 250 up to 2500. The formulations included the vortex method, unsteady equations in streamfunction form, steady equations and the associated linear stability problem, and the unsteady equations in primitive variable form. The numerical methods used cover almost all of the existing schemes in the literature. The majority of the numerical results are summarized in [24]. The work of Gresho *et al.* was an answer to a controversy concerning the stability of the stationary solution at $Re = 800$. It was concluded by Kaiktsis *et al.* [25] that transition to turbulent flow has occurred at $Re = 800$. Kaiktsis *et al.* examined the long-time temporal behavior of the flow and found that the flow is steady at $Re = 500$, time periodic at $Re = 700$, and chaotic at $Re = 800$. Gresho *et al.* did a detailed grid refinement study using four different numerical methods and concluded that the backward-facing step at $Re = 800$ is a stable steady flow.

In addition to the study of Gresho *et al.*, an extensive grid refinement study of this flow using a spectral element method was conducted in [26]. The simulated geometry and the numerical method corresponds to that of Kaiktsis *et al.* [25], and flow was examined at Reynolds numbers of 500 and 800. His systematic grid refinement study was performed by varying both the element size and the order of the polynomial representation within the elements. For both Reynolds number values with the transient computations stopped at $t = 800$, it was observed that low resolution grid cases exhibit chaotic-like temporal behavior, whereas high resolution grid cases evolve toward asymptotically steady flow by a monotonic decay of the transient. The resolution required to obtain asymptotically steady behavior is seen to increase with Reynolds number. These results suggest that the reported transition to sustained chaotic flow [25] at Reynolds numbers around 700 is an artifact of inadequate spatial resolution. Torczynski's conclusion was further confirmed by a subsequent study of Kaiktsis *et al.* [27] and Fortin *et al.* [28]. Fortin *et al.* employed tools from dynamical systems theory to search for the Hopf bifurcation point (transition point). They showed that the backward-facing step remains a steady flow at least up to $Re = 1600$. The purpose of the present study is to refine the study of Torczynski [26] using dynamical systems theory to interpret the results. The next two sections give details of Torczynski's analysis and the present study.

3.2. Grid refinement study of [26]

In [26], the $\mathrm{Re} = \rho\bar{u}2h/\mu$ is based on upstream conditions. The variable $\bar{u}$ is the spatial average of the horizontal velocity u over h. The geometry is specified to match that of Kaiktsis *et al.* [25]. The upstream channel height h and step height s have values of $h = 1$ and $s = 0.94231$, yielding a downstream channel height of $H = 1.94231$. The corner of the step is at $(x, y) = (1, 0)$. The channel extends a distance $l = 1$ upstream from the step and a distance $L = 34$ downstream from the step to preclude undue influence of the finite channel length on the flow at $Re = 800$. The following conditions are applied on the boundaries of the computational domain: $u = v = 0$ on the upper and lower channel walls, $-p + \mu\,\partial u/\partial n = 0$ and $\partial v/\partial n = 0$ on the outflow boundary, and $u = [\tanh(t/16)]u_{\mathrm{B}}(y) + [1-\tanh(t/16)]u_{\mathrm{P}}(y)$ and $v = 0$ on the inflow boundary and the step surface. Here, $u_{\mathrm{B}}(y) = \max[0, 3y(1-y)]$ is the correct boundary condition for flow over a backward-facing step and $u_{\mathrm{P}}(y) = 3(1-y)(s+y)/(1+s)^3$ is the Poiseuille flow observed infinitely far downstream whenever steady flow is asymptotically obtained. The initial velocity field is set equal to $u = u_{\mathrm{P}}(y)$ and $v = 0$ throughout the domain. Here v is the vertical velocity and p is the pressure. Thus, the above combination of boundary and initial conditions initially allows flow through the step surface so that the simulations can be initialized using an exact divergence-free solution of the Navier–Stokes equations. Furthermore, since the inflow boundary condition is varied smoothly in time from Poiseuille flow to flow over a backward-facing step, the flow experiences an order unity transient that is probably strong enough to excite sustained unsteady behavior, if that is the appropriate asymptotic state for the numerical solution.

The simulations were performed using the commercial code NEKTON v2.8, which employs a time-accurate spectral element method with the Uzawa formulation [29]. Let D be the dimensionality. Each element has N^D velocity nodes located at Gauss–Lobatto Legendre collocation points, some of which are on the element boundaries, and $(N-2)^D$ pressure nodes located at Gauss Legendre collocation points, all of which are internal. Within each element, the velocity components and the pressure are represented by sums of D-dimensional products of Lagrangian interpolant polynomials based on nodal values. This representation results in continuous velocity components but discontinuous pressure at element boundaries. Henceforth, the quantity N is referred to as the element order, even though the order of the polynomials used to represent the velocity is $N-1$. NEKTON employs mixed explicit and implicit temporal discretizations. To avoid solving a non-linear non-symmetric system of equations at each time step, the convective term is advanced explicitly in time using a third-order Adams–Bashforth scheme. All other terms are treated implicitly (backward Euler for the pressure and for the viscous terms).

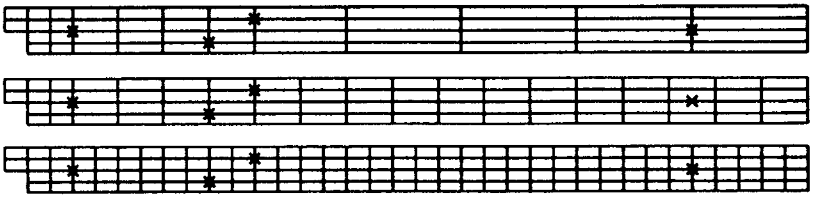

Figure 4. Distribution of the spectral element grids (the distribution of the nodes within each spectral element is not shown): L grid: top; M grid: middle; H grid: bottom. Velocity and pressure histories are recorded at points (3, 0), (9, −0.5), (11, 0.5) and (30, 0), marked by crosses (×).

Three spectral element grids of differing resolution, denoted L (low), M (medium) and H (high), are employed. Figure 4 shows the computational domain and the grid distribution of the three spectral element grids in which the *distribution of nodes within each spectral element is not shown*. The L grid with $N=9$ is identical to the grid of Kaiktsis *et al.* [25]. Tables I and II show the results for a fixed time step of $\Delta t = 0.10$ at $t = 800$. This time step appears to satisfy the Courant restriction of the explicit portion of the temporal discretization. Four general classes of behavior are observed for the numerical solutions. First, 'steady monotonic' denotes evolution of the numerical solution toward an asymptotically steady state. Second, 'steady oscillatory' denotes evolution toward an asymptotically steady state with a decaying oscillation superimposed on the monotonic decay. Third, 'unsteady chaotic' denotes irregular transient behavior of the numerical solution that shows no indication of evolving toward steady behavior. Fourth, 'diverge' denotes a numerical solution terminated by a floating-point exception. In Tables I and II, the first character under the 'case' columns denotes the grid resolution L, M or H, the first number indicates the Reynolds number 500 or 800 and the last two numbers indicate the order of the spectral element being used. For example, $L807$ means $Re = 800$ using the L grid with $N = 7$.

The extensive grid refinement study of Torczynski resulted in grid-independent steady state numerical solutions for both $Re = 500$ and $Re = 800$. As the grid resolution is reduced below the level required to obtain grid-independent solutions, chaotic-like temporal behavior occurred. The degree of grid resolution required to obtain a grid-independent solution was observed to increase as the Reynolds number is increased.

Table I. Mesh refinement results for $Re = 500$ at $t \leq 800$

Case	Grid	N	Temporal behavior
$L505$	L	5	Diverge
$L506$	L	6	Unsteady chaotic
$L507$	L	7	Unsteady chaotic
$L508$	L	8	Steady oscillatory
$L509$	L	9	Steady monotonic
$M505$	M	5	Diverge
$M506$	M	6	Steady monotonic
$M507$	M	7	Steady monotonic
$H505$	H	5	Steady monotonic
$H507$	H	7	Steady monotonic

Table II. Mesh refinement results for $Re = 800$ at $t \leq 800$

Case	Grid	N	Temporal behavior
$L809$	L	9	Diverge
$L811$	L	11	Unsteady chaotic
$M805$	M	5	Diverge
$M806$	M	6	Diverge
$M807$	M	7	Steady chaotic
$M808$	M	8	Steady oscillatory
$M809$	M	9	Steady monotonic
$H805$	H	5	Diverge
$H806$	H	6	Steady monotonic
$H807$	H	7	Steady monotonic
$H808$	H	8	Steady monotonic
$H809$	H	9	Steady monotonic

3.3. Interpretation of Torczynski's result using dynamical systems theory

The purpose of the present study is not to reaffirm Torczynski's study, or to target the spectral element method, or the work of Kaiktsis *et al.* [25], but rather to allude to how easily, without a grid refinement study and knowledge of dynamical systems theory, similar erroneous conclusions could possibly arise in other CFD practices. As stated before, inaccuracy associated with underresolved grids (e.g. disappearance of the fine details of the flow due to large numerical diffusion and/or low order of the scheme) and linear instability associated with time discretizations are easier to detect than spurious numerical solutions. With the knowledge of possible non-linear behavior of numerical schemes, such as long-time transients before a steady state is reached, numerically induced chaotic transients, numerically induced or suppressed chaos, existence of spurious steady states and asymptotes, and the intimate relationship among initial data, time step and grid spacing observed in discrete dynamical systems theory, we need to examine these cases in more detail. They can serve to illustrate the connection between the spurious numerics phenomena observed in simple non-linear models and CFD computations.

In the present study, further refinements are made on all of the underresolved grid cases in Tables I and II to determine if these cases sustain the same temporal behavior at a much later time or evolve into a different type of behavior. At $t = 800$, cases $L506$, $L507$, $L508$, $L509$, $L811$, $M807$ and $M808$ either exhibit 'unsteady chaotic' or 'steady oscillatory' behavior. These cases are increased to $t = 2000$ to determine if a change in solution behavior occurs. From the phenomena observed in [21] and others, $t = 2000$ might not be long enough for a long-time transient or long-chaotic transient to die out. There is also the potential of evolving into a different type of spurious or divergent behavior at a much later time. However, for this study, it appears that $t = 2000$ is sufficient. For $Re = 500$, the authors also recomputed some of these cases with a sequence of Δt that bracketed the benchmark study of Torczynski. The Δt values are 0.02, 0.05, 0.10, 0.125, 0.2, 0.3, 0.4 and 0.5 for $Re = 500$. The CFL number for all of these cases is above 1 for $\Delta t > 0.10$. The reason for the investigation of $\Delta t = 0.3$, 0.4 and 0.5 is to find out, after the transients have died out, if the solution converges to the correct steady state for Δt that are a few times larger than 0.10.

For $Re = 800$, $L811$ and $M808$ are integrated with $\Delta t = 0.10$ and $M807$ with $\Delta t = 0.02$, 0.05 and 0.10 to $t = 2000$. Aside from integrating to $t = 2000$, five different initial data were examined for cases $M807$, $M809$ and $M811$ for $\Delta t = 0.10$ to determine the influence of the initial data and the grid resolution on the final numerical solution. The five initial data are:

Table III. Mesh refinement results for $Re = 500$ at $t \leq 2000$

Case	Grid	N	Temporal behavior
L505	L	5	Diverge
L506	L	6	**Time periodic**
L507	L	7	**Time periodic**
L508	L	8	Steady oscillatory
L509	L	9	Steady oscillatory
M505	M	5	Diverge
M506	M	6	Steady monotonic
M507	M	7	Steady monotonic
H505	H	5	Steady monotonic
H507	H	7	Steady monotonic

(a) Uniform: $u, v = 0$.
(b) Shear layer: $u = u_B(y) = \max[0, 3y(1-y)]$, $v = 0$.
(c) Solution from solving the steady Stokes equation (with no convection terms).
(d) [26]: $u = u_P(y) = 3(1-y)(s+y)/(1+s)^3$, $v = 0$.
(e) Channel flow both upstream and downstream of step: same as (d) except the boundary conditions.

The boundary conditions for (a), (b), (c) and (e) were parabolic inflow and no-slip at walls, whereas the boundary conditions for (d) were those of Torczynski [26]: $u = [\tanh(t/16)]u_B(y) + [1 - \tanh(t/16)]u_P(y)$ and $v = 0$. The CPU required to run the above cases ranged from less than a day to several days on a Sparc Center 2000 using one processor.

The solution behaviors reported in Tables I and II, with additional refinement study, now become Tables III and IV. Note that the 'steady monotonic' cases in Tables III and IV are at $t = 800$ and the rest are at $t = 2000$ (if a divergent solution has not occurred earlier). The chaotic-like behavior evolves into a time periodic solution beyond $t = 800$ for L506 and L507, whereas the chaotic-like behavior evolves into a time periodic solution beyond $t = 800$ for L811 and a divergent solution for M807. The 'steady oscillatory' case L508 is slowly evolving to the correct steady state with an amplitude of oscillation of 10^{-5}. The oscillation is not

Table IV. Mesh refinement results for $Re = 800$ at $t \leq 2000$

Case	Grid	N	Temporal behavior
L809	L	9	Diverge
L811	L	11	**Time periodic**
M805	M	5	Diverge
M806	M	6	Diverge
M807	M	7	**Diverge**
M808	M	8	Steady oscillatory
M809	M	9	Steady monotonic
H805	H	5	Diverge
H806	H	6	Steady monotonic
H807	H	7	Steady monotonic
H808	H	8	Steady monotonic
H809	H	9	Steady monotonic

Table V. Initial data study for $Re = 800$ and M grid at $t \leq 2000$

ICs	M807	M809	M811
a	Diverge	Diverge	Diverge
b	Diverge	Steady montonic	Steady montonic
c	Diverge	Diverge	Diverge
d	Diverge	Steady montonic	Steady montonic
e	Diverge	Diverge	Diverge

detectable within the plotting accuracy. The 'steady oscillatory' time evolution of M808 is similar to that of L508. The numerical solutions with 'steady oscillatory' and 'steady monotonic' behavior at early stages of the time integration are almost identical at later stages of the time integration. They all converge to the correct steady state. The initial data study at $Re = 800$ with $\Delta t = 0.10$ is summarized in Table V. It illustrates the intimate relationship between initial data and grid resolution.

Figure 5 shows the streamlines for L509 (steady state solution) and L507 (spurious time periodic solution). Figure 6 shows the streamlines for H809 (steady solution) and L811 (spurious time periodic solution) and the corresponding grids with the distribution of the nodes of the spectral elements shown. Note that even for the L grid using $N = 11$ (L811), the grid spacings are very fine and yet a spurious time periodic solution was obtained.

Figures 7–10 show the vertical velocity time histories at $(x, y) = (30, 0)$ advanced to a time of $t = 2000$ of selected runs for both Reynolds numbers and various Δt. They illustrate the different spurious behaviors of the underresolved grid cases at $t < 2000$. The amplitude of the spurious time periodic solutions remains uniform for L506 for $0.02 \leq \Delta t < 0.2$ (Figure 7) but not for L507 (Figure 8). A counter-intuitive behavior was observed for the L507 case. For L507, the amplitude of the spurious time periodic solution remains constant for $\Delta t = 0.02$ and 0.05 but decreases to a significantly lower value for the large time step range. One would expect the opposite effect on the height of the amplitude. In addition, the two distinct amplitudes of the periodic solution indicate the existence of two finite ranges of Δt, where the numerical solutions converge to two distinct spurious time periodic solutions for L507.

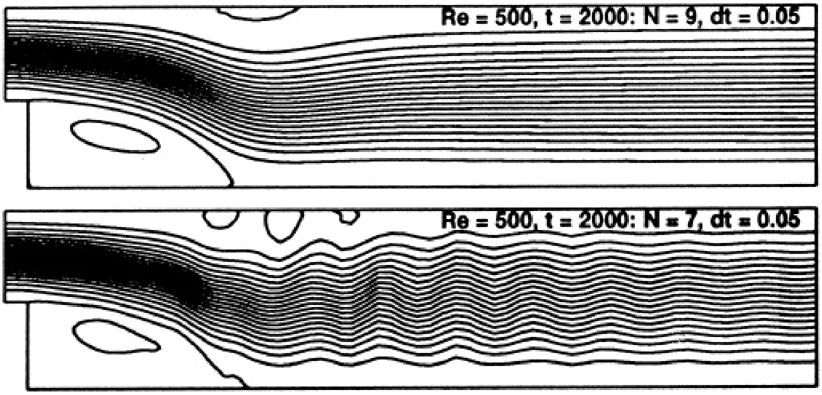

Figure 5. Streamlines for L509 (steady) and L507 (spurious time periodic) cases (vertical scale expanded four times for viewing).

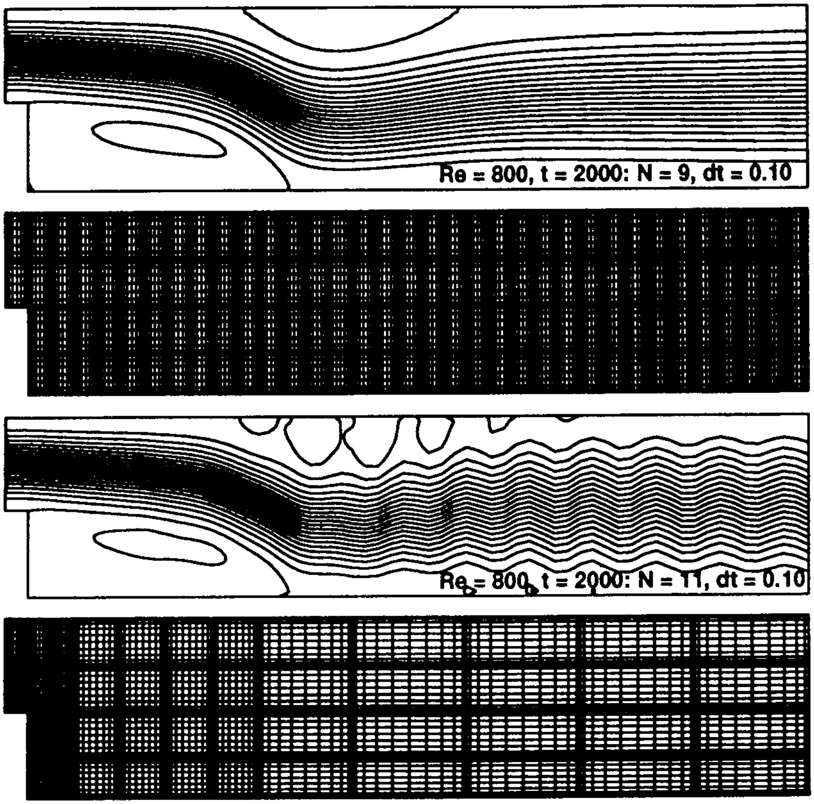

Figure 6. Streamlines for $H809$ (steady) and $L811$ (spurious time periodic) and the corresponding grids (vertical scale expanded four times).

Figure 10 shows the vertical velocity time histories at $(x, y) = (30, 0)$ for $M807$ with $\Delta t = 0.02$, 0.05 and 0.10, and $L811$ for $\Delta t = 0.10$. Case $M807$ diverges at $t = 1909.2$ for $\Delta t = 0.02$, at $t = 972.4$ for $\Delta t = 0.05$, and at $t = 827.77$ for $\Delta t = 0.10$. The time histories for these three time steps appear to show chaotic-like behavior if one stops the computations at $t = 800$. The bottom plot of Figure 10 shows the vertical velocity time histories advanced to a time of $t = 2000$ for $L811$ with $\Delta t = 0.10$. It shows the definite time periodic spurious solution pattern. On the other hand, the time history for this case appears to show an aperiodic-like pattern if one stops the computation at $t = 800$. Note that the $L809$ grid case was used by Kaiktsis *et al.* [25] and they concluded that transition has occurred at $Re = 800$.

In summary, without the longer time integration, the $L506$, $L507$, $L811$ and $M807$ cases can be mistaken to be chaotic-like (or aperiodic-like) flow. Although the time history up to $t = 800$ appears chaotic-like, one cannot conclude it is chaotic without longer transient computations. Comparing Tables I and II with Tables III, IV and V, one can conclude that with transient computations that are 2.5 times longer than Torczynski's original computations, what appeared to be aperiodic-like or chaotic-like behavior at earlier times evolved toward either a time periodic or divergent solution at later times. These temporal behaviors appear to be long-time aperiodic-like transients or numerically induced chaotic-like transients. For $Re =$ 800, five different initial data were examined to determine if the flow exhibits strong dependence on initial data and grid resolution. Results showed that the numerical solutions are sensitive to these five initial data. The refinement study also revealed a non-standard guideline in grid clustering or grid adaptation. Traditional grid refinement and grid adaptation methods concentrate on regions with strong gradients, shock waves, slip surfaces and fine structure of the flow, and de-refine regions of smooth flows. As can be seen in Figures 5 and 6, the flow downstream of the backward-facing step is very smooth, yet a fine grid is needed in this region in order to obtain the correct numerical solution. It is postulated that proper non-linear wave propagation is hampered by the underresolved grid. This behavior may be related to spurious discrete traveling waves. A separate investigation is needed and is beyond the scope of the present paper. See [1,8] for a discussion. A suggestion to minimize spurious asymptotes is discussed in References [4,9,16]. Note that the results presented pertain to the characteristic of the studied scheme and the DNS computations. See also [23] for the characteristic of spurious bifurcations of other time integrators. However, if one is certain that $Re = 800$ is a stable steady flow, a non-time-accurate method such as time marching to obtaining the steady state numerical solution would be a more efficient numerical procedure.

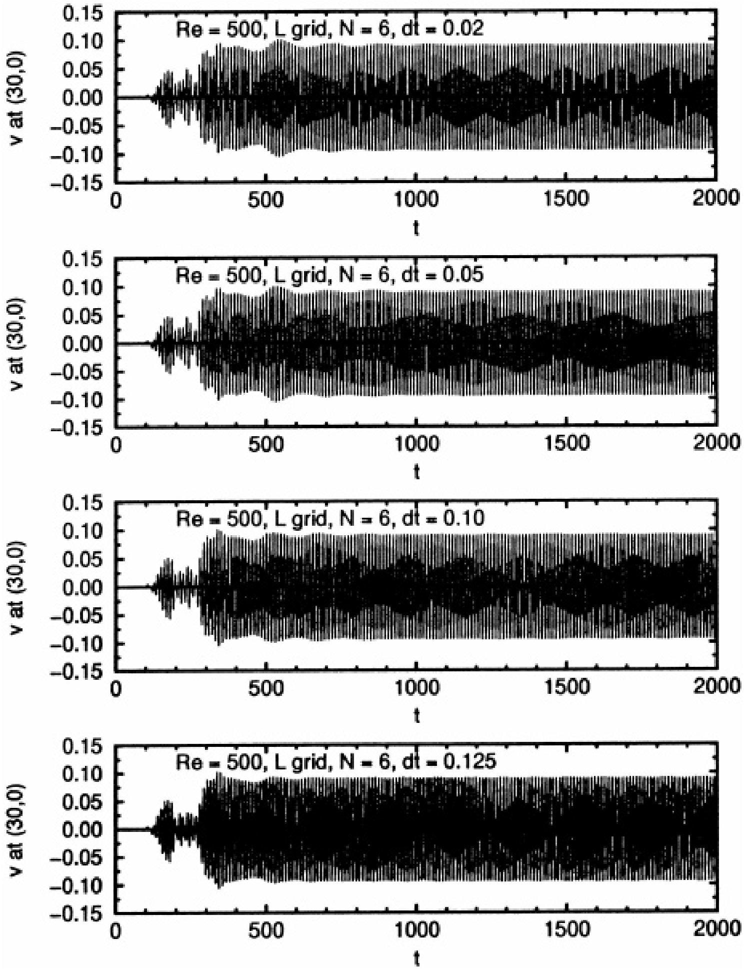

Figure 7. Vertical velocity time histories for $L506$ ($Re = 500$, $N = 6$, L grid) with $\Delta t = 0.02$, 0.05, 0.10 and 0.125.

4. TIME LAG COUPLING OF A FLUID–STRUCTURE INTERACTION

This section discusses the spurious behavior of a third type of semi-implicit method. This type of semi-implicit method is commonly used in combustion and fluid–structure interaction analysis. These type of problems are commonly mathematically stiff and highly non-linear, and consist of a large number of strongly coupled equations. The simulation considered employs the unsteady 2D compressible Navier–Stokes equations coupled with a two-equation elastic model on overlapping grids involving stationary and deforming meshes.

A common practice in time-accurate aeroelastic computations is to utilize well-validated implicit Navier–Stokes algorithms that were developed for complex flow fields over 3D non-deforming bodies and extend them to include aeroelastic effects. The simplest approach to extend these algorithms is to lag the effects of moving/deforming structures by one time step [30–32], allowing current algorithms to be used in updating the aerodynamic variables. After the aerodynamic loads are determined, a structural module is called to update the position and

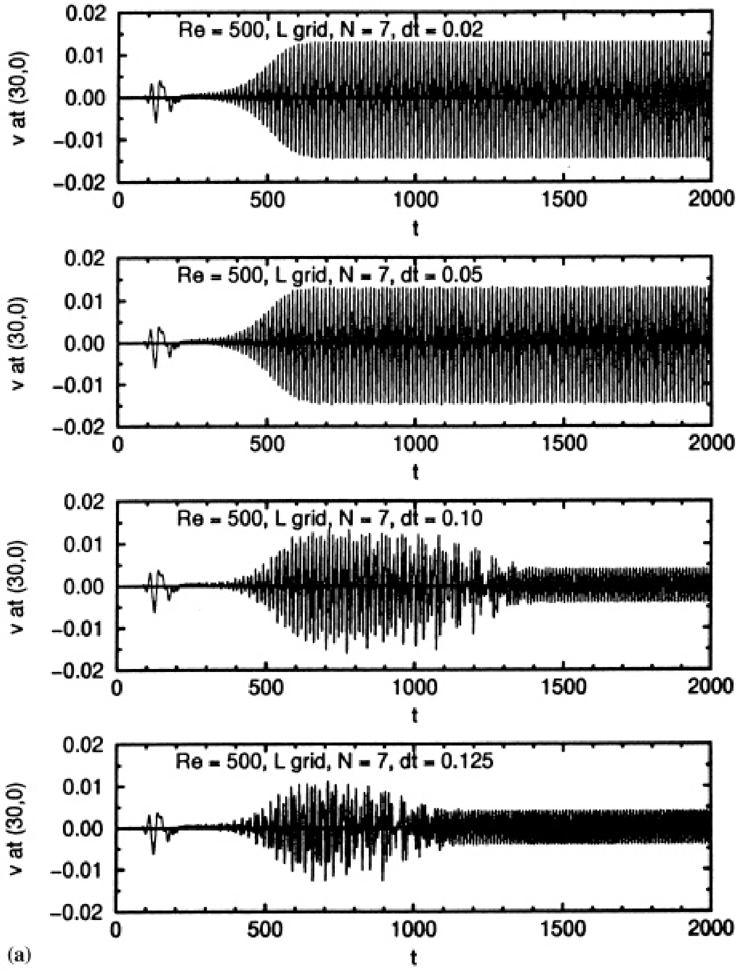

Figure 8. Vertical velocity time histories for $L507$ ($Re = 500$, $N = 7$, L grid) with $\Delta t = 0.02$, 0.05, 0.10, 0.125, 0.2, 0.3, 0.4 and 0.5.

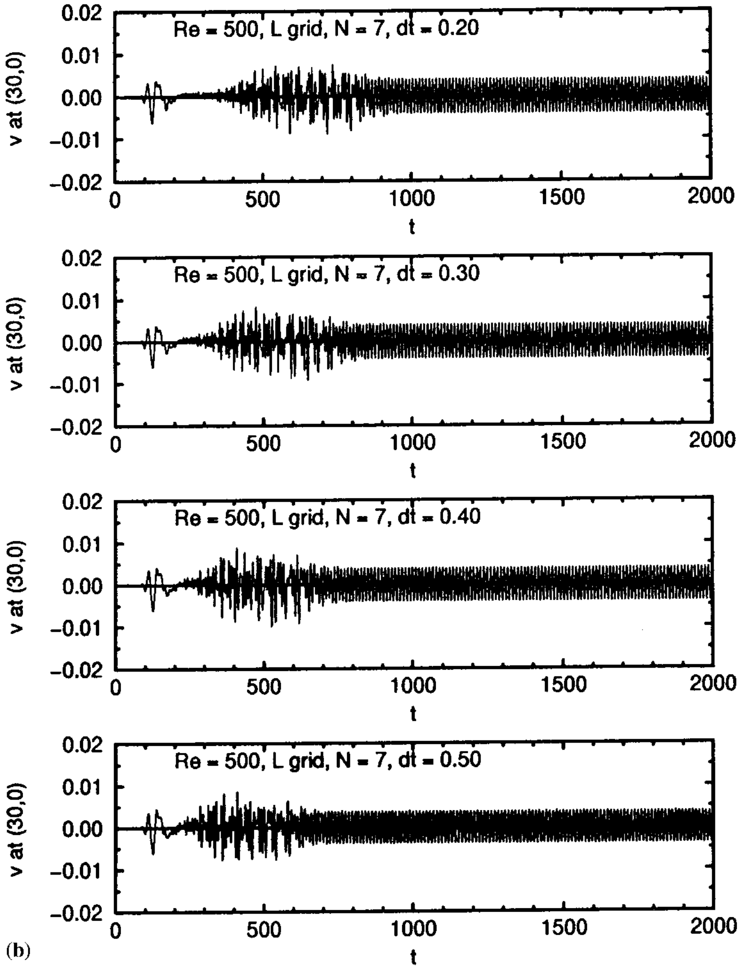

Figure 8 (*Continued*)

shape of the body. A disadvantage of this semi-implicit strategy is the fact that regardless of the temporal accuracy of the aerodynamic and structural algorithms, the loose coupling introduces an $O(\Delta t)$ error, and may impose more stringent stability criteria. Besides introducing undesirable phase lag, it may also introduce spurious solutions as a result of the semi-implicit procedure.

4.1. Elastically mounted cylinder

An elastically mounted cylinder model problem is used to demonstrate the occurrence of spurious solutions when using the lagged structures approach. A circular cylinder is mounted in a free-stream of velocity V_∞ with linear springs in both co-ordinate directions as depicted in Figure 11. The aeroelastic cylinder is an attractive model problem for two reasons. First, it displays non-linear unsteady flow field physics associated with separation and vortex shedding, and, second, there are both numerical and experimental data available for comparison [33,34].

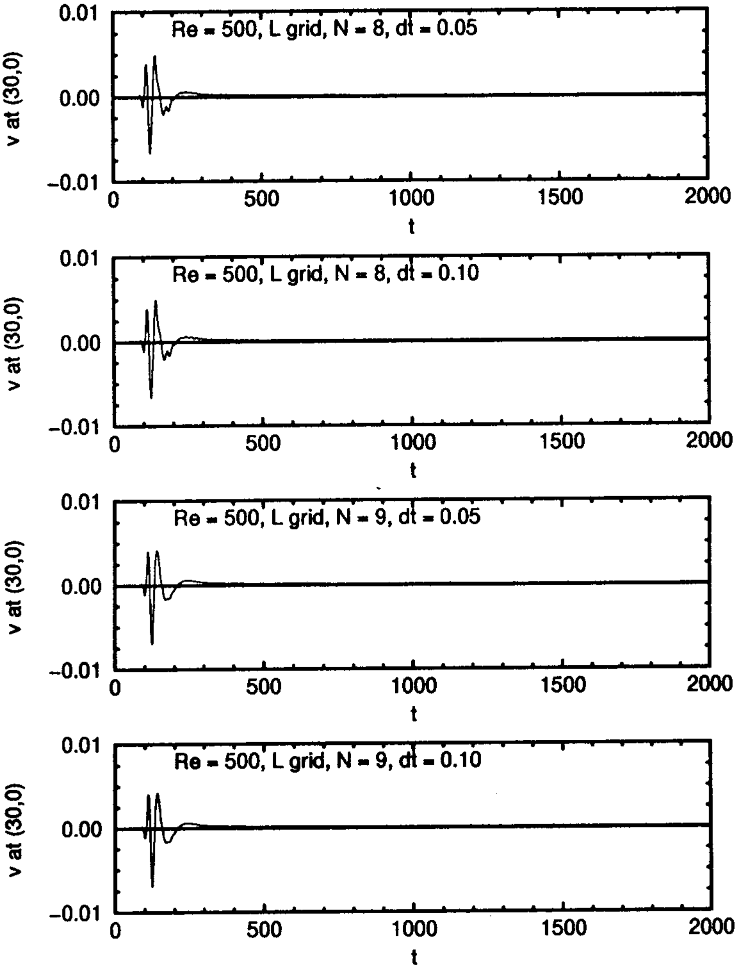

Figure 9. Vertical velocity histories for $L508$ and $L509$ with $\Delta t = 0.05$ and 0.10.

The governing equations used to model the aerodynamic system are the compressible laminar Navier–Stokes equations. The governing equations for the 2 degrees of freedom model [33,34] in dimensional form are

$$m\ddot{x}_{\text{ea}} + C\dot{x}_{\text{ea}} + Kx_{\text{ea}} = D, \tag{4.1}$$

$$m\ddot{y}_{\text{ea}} + C\dot{y}_{\text{ea}} + Ky_{\text{ea}} = L, \tag{4.2}$$

where m, C, K, D and L are the mass, coefficient of structural damping, coefficient of spring stiffness, drag and lift per unit span respectively, and x_{ea} and y_{ea} are the horizontal and vertical positions of the center of the cylinder.

The governing equations are solved on a deforming mesh overlapping a stationary mesh with a Beam–Warming approximate factored algorithm modified to include Newton-like subiteration of index p, coupled with an ordinary differential equation structural solver, also in subiteration form. The temporal discretization is either the backward Euler (first-order) or the three-point backward differentiation (three-point BDF, second-order) and is linearized about the solution at subiteration level *p*. The spatial derivatives of the Navier–Stokes equations are approximated by second-order central differences and common forms of both implicit and explicit non-linear dissipation. With a sufficient number of subiterations, this approach becomes a fully implicit first- or second-order accurate aeroelasticity solver. All solutions of this work were computed using the backward Euler temporal discretization without subiteration to model a lagged structures approach. The solutions were then compared with the solutions of the fully implicit approach. Details of the solver can be found in [35]. Morton *et al.* illustrate the importance of using the fully coupled, fully implicit second-order approach for the fluid–structure interaction. Surface boundary conditions are comprised of no-slip, adiabatic wall and the inviscid normal momentum equation. Free-stream conditions are specified along the outer boundary inflow and extrapolation in the horizontal co-ordinate is implemented at the outer boundary outflow. Periodic conditions are applied along the overlap boundary (due to the *O* grid topology). The method's accuracy was verified through comparison with numerical and experimental solutions reported in [35].

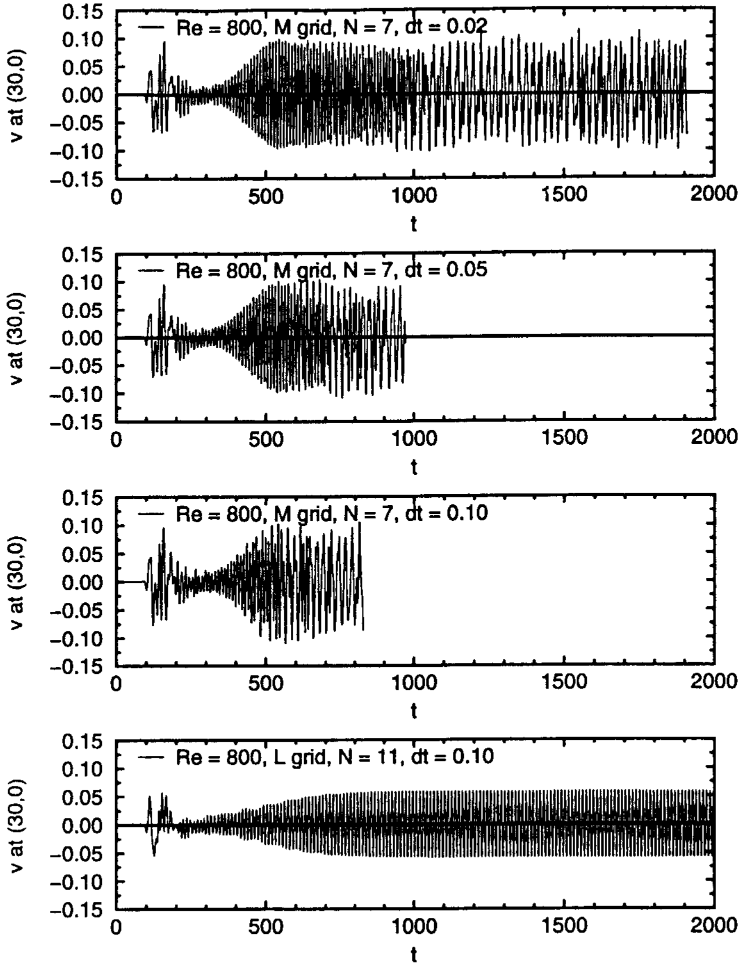

Figure 10. Vertical velocity time histories for $M807$ with $\Delta t = 0.02$, 0.05 and 0.10, and $L811$ with $\Delta t = 0.10$. (Case $M807$ diverges at $t = 1909.2$ for $\Delta t = 0.02$, at $t = 972.4$ for $\Delta t = 0.05$, and at $t = 827.77$ for $\Delta t = 0.10$.)

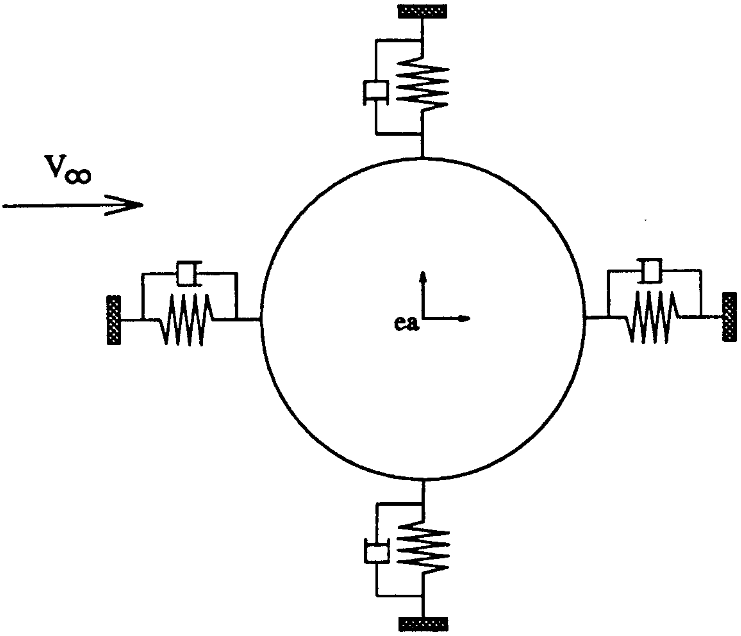

Figure 11. Aeroelastic cylinder model.

4.2. *Numerical results*

Elastically mounted cylinder solutions were computed for a variety of time steps with the lagged structures/no subiteration approach. The baseline structural parameters used for all cases were

$$Re = 500, \quad M_\infty = 0.2, \quad \zeta = 1, \quad \mu_s = 5, \quad \bar{u} = 4, \tag{4.3}$$

where ζ is the non-dimensional structural damping coefficient, μ_s is the mass ratio and $\bar{u}$ is the reduced velocity. See [35] for details of the physical parameters. The computational grid has 384 evenly spaced points around the cylinder, and 96 points in the radial direction. A non-dimensional spacing of 0.0005 was specified normal to the surface, and the grid was geometrically stretched to a maximum radius of 50 cylinder diameters.

The fluid–structure interaction system was initialized by computing a static cylinder time periodic solution with a time step of $\Delta t = 0.01$. Once this solution was determined to be periodic, the cylinder was allowed to move in both co-ordinate directions in response to the periodic shedding of vortices. The cylinder established a new periodic solution characterized by oscillations in the x and y co-ordinates of the cylinder center. This initial periodic solution was then used to compute a set of solutions for increasing and decreasing time steps.

Refinement in time step produced an asymptotic solution with a non-dimensional frequency (Strouhal number) of $St = 0.2256$. Solutions for the most refined time step up to a time step of 0.02 were sinusoidal with a single frequency and amplitude. As the time step was increased in this range, the amplitude of vertical motion increased and the frequency of oscillation decreased monotonically. Solutions for time steps greater than 0.02 have additional frequency content not evident in the smaller time step solutions. To determine the frequency content, a power spectral density (PSD) analysis was performed with MATLAB.

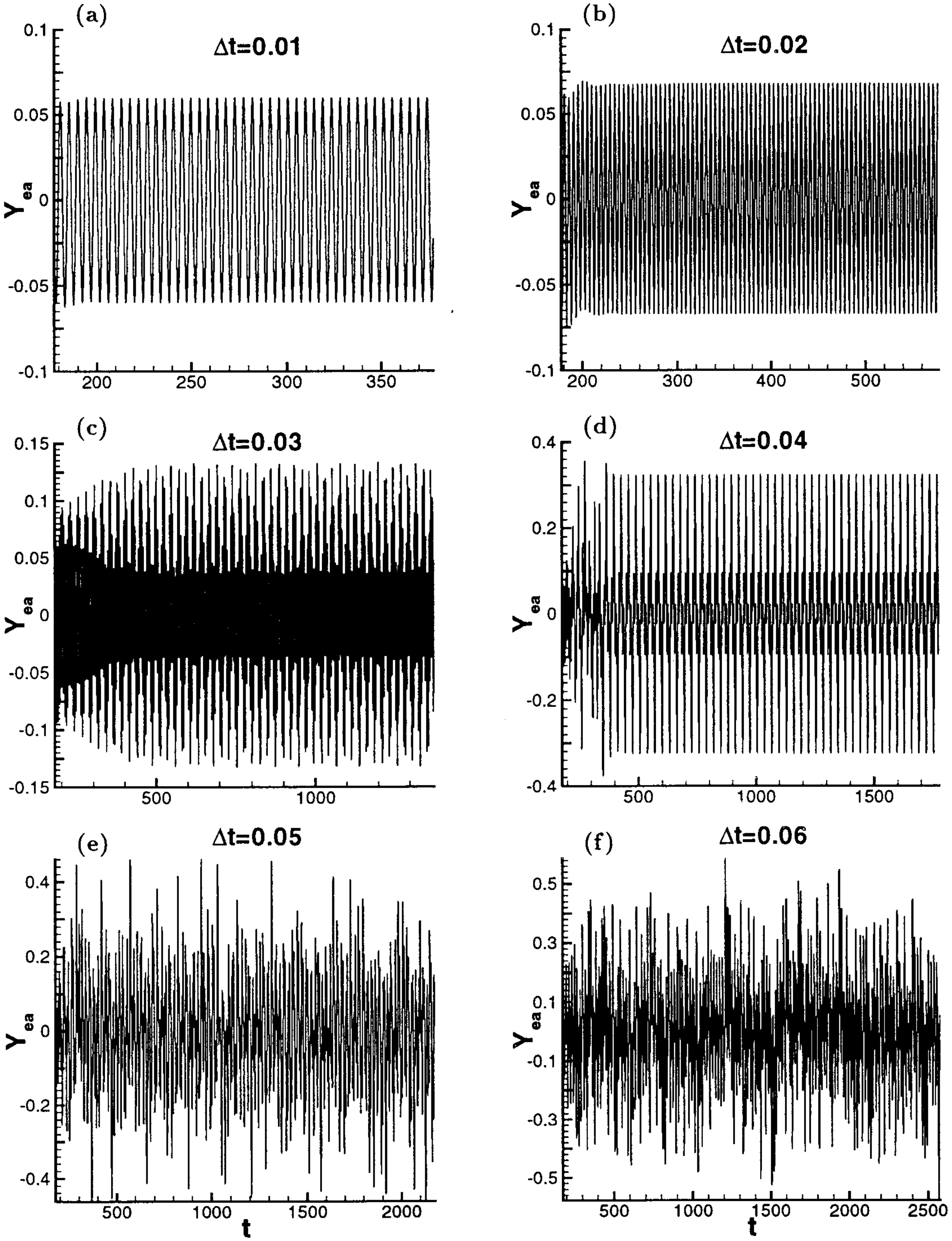

Figure 12. Circular cylinder vertical motion time histories for the lagged structures for $\Delta t = 0.01$, 0.02, 0.03, 0.04, 0.05, 0.6 ($Re = 500$, $M_\infty = 0.2$).

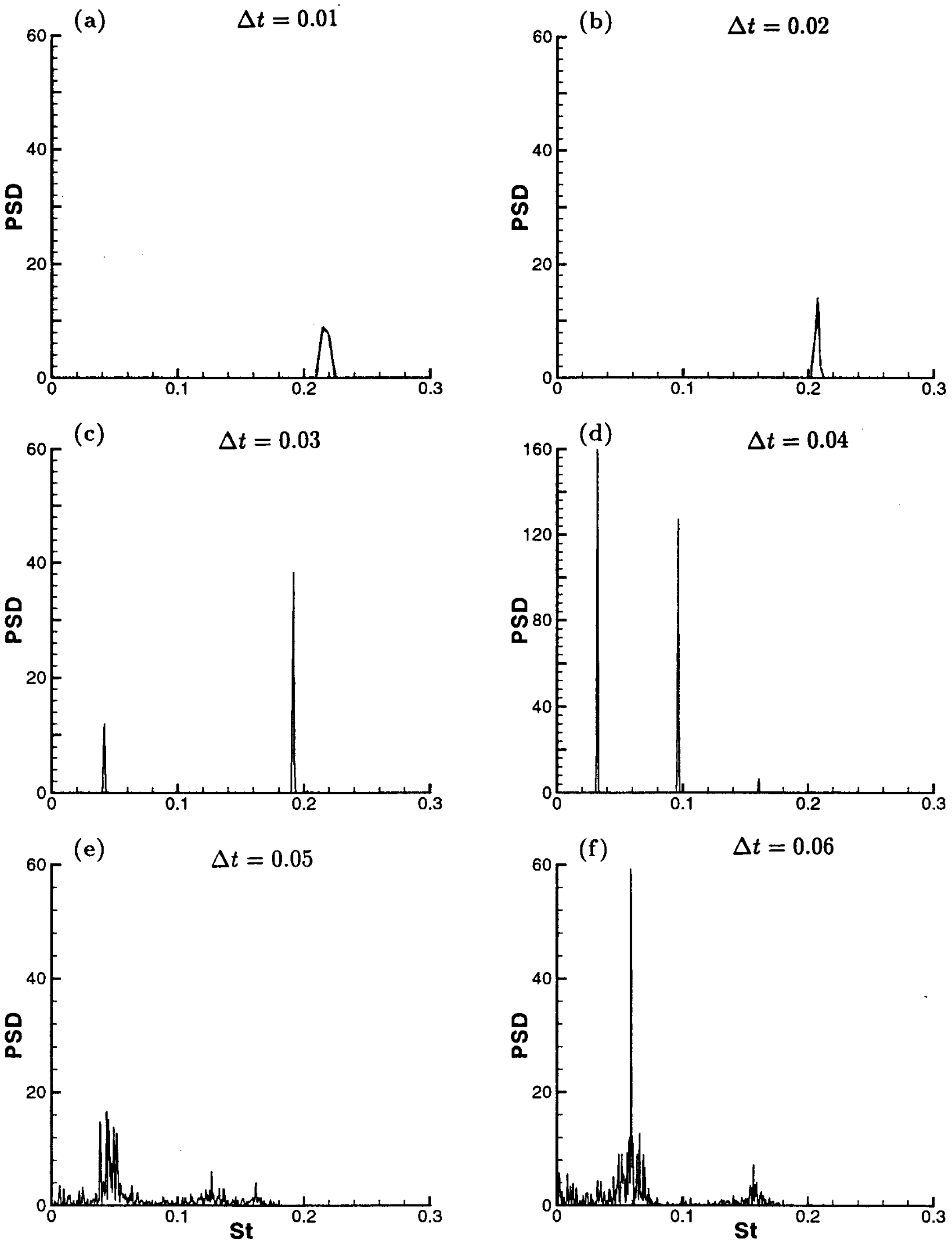

Figure 13. Power spectral density (PSD) vs. Strouhal number for the lagged structures for $\Delta t = 0.01$, 0.02, 0.03, 0.04, 0.05, 0.06 ($Re = 500$, $M_\infty = 0.2$).

Figures 12 and 13 show the cylinder center vertical motion time histories and the corresponding PSD analysis for six different time steps ($0.01 \leq \Delta t \leq 0.06$ with an increment of 0.01). The length of the total time integrations, determined by monitoring the time evolution solution behavior, increases as Δt increases. The total time integrations for the six time steps are $t = 380$, 900, 1400, 1800, 2200 and 2600 respectively. The lengths of these time integrations are also guided by the knowledge gained from previous sections and References [9,16]. It is interesting to see the various spurious behavior as a function of Δt. The form of the solutions evolves from a sinusoidal periodic solution to periodic solutions with more than one frequency, and eventually to aperiodic/chaotic-like patterns.

Figure 13(a) and (b) show the single frequency associated with time steps of 0.01 and 0.02 with a trend toward lower frequency with increasing time step. The amplitudes of the sinusoidal motion are affected by the size of the Δt. The PSD analysis for the $\Delta t = 0.03$ solution (Figure 13(c)) shows the same trend for the dominant frequency but an additional lower frequency component is evident. This additional spurious frequency is responsible for the aperiodic-like motion of the cylinder (Figure 12(c)).

It is interesting to note the change in character of the solution for $\Delta t = 0.04$ (Figure 12(d)). The solution is time periodic with several distinct local minima and maxima within one cycle. The PSD analysis shows three distinct frequencies (Figure 13(d)) with the two spurious low frequencies dominating the frequency closest to the asymptotic solution frequency.

The solutions for $\Delta t = 0.05$ and 0.06 (Figure 12(e) and (f)) are chaotic-like. The PSD analyses (Figure 13(e) and (f)) for both time steps show a spectrum of frequencies as opposed to the few distinct frequencies seen in lower Δt solutions. The dominant frequencies are similar for both time step solutions with the $\Delta t = 0.06$ solution showing very large PSD in the low frequency range.

These time histories indicate a counter-intuitive behavior. The solution changes from a periodic pattern for $\Delta t = 0.02$ to an aperiodic pattern for $\Delta t = 0.03$, and then back to a periodic pattern for $\Delta t = 0.04$ before the onset of chaotic-like behavior for $\Delta t = 0.05$ and 0.06.

Solutions were computed with the fully coupled approach with subiterations to determine if spurious solutions were evident at the same time steps. Figure 14 depicts a comparison of fully

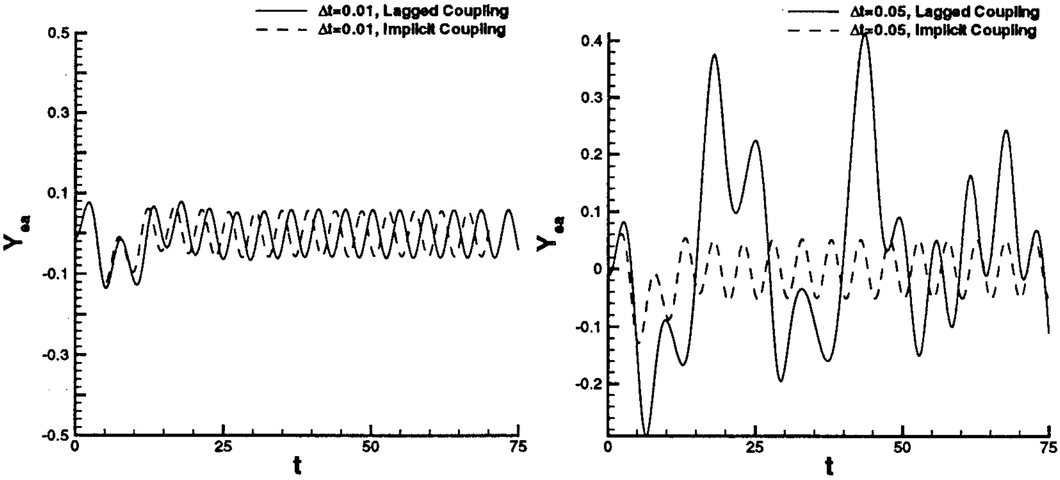

Figure 14. Circular cylinder vertical motion time histories for fully coupled and lagged structures for $\Delta t = 0.01$ and 0.05.

implicit versus lagged structures solutions for $\Delta t = 0.01$ and 0.05. The spurious behavior was not evident for $\Delta t = 0.05$ for the fully implicit approach. In addition to the spurious behavior manifested by the lagged structures for slightly larger time steps, smaller time steps, although producing the correct solution, exhibit a time lag over the fully coupled case.

In summary, for time steps greater than 0.02, the model exhibits spurious solutions when the loosely coupled implicit approach is employed. In some cases the numerical solutions were not chaotic but were still spurious and time periodic, making it difficult for the researcher to determine if the solution is representative of the true physics of the problem. Fortunately, a fully implicit structural coupling eliminated the spurious solutions for time steps much greater than those associated with the spurious lagged structures solutions for the given model problem. Large scale full aircraft computations are expensive, and therefore it is tempting for researchers to trade efficiency for accuracy by increasing the time step. This may lead to spurious solutions that are difficult to detect without a comprehensive time step refinement study.

5. 3D COMPRESSIBLE FLOW SIMULATIONS OF VORTEX BREAKDOWN ON DELTA WINGS

This section discusses the spurious behavior of underresolved grids observed in [36–38] using the backward Euler fully implicit temporal discretization for a 3D vortex breakdown on delta wings. For certain initial angles of attack, spurious time periodic and spurious chaotic-like temporal behavior occurs as the grid resolution is reduced. The coarse grid used is actually finer than grids commonly used in full aircraft simulations. In view of the fact that some experimental studies have reported the existence of vortex breakdown static hysteresis on delta wings and others have not, the coarse grid case could be mistaken to exhibit similar non-unique solutions behavior to that of some of the experimental data if a grid refinement study is not made.

5.1. Flow configuration, governing equations and numerical procedure

The vortical flows encountered by agile aircraft at high angle of attack exhibit a variety of complex, non-linear aerodynamic phenomena not yet fully understood. Among these is ‘vortex breakdown’ or ‘vortex bursting’, which represents a sudden disruption of the well-organized leading edge vortex present above slender wings at high incidence. Vortex breakdown is typically characterized by reverse axial flow in the vortex core, and by marked flow fluctuations downstream of the breakdown inception location. The sudden onset of vortex breakdown and its effects on aerodynamic loads severely impact aircraft stability and control and may result in reduction of the operational envelope of high performance aircraft. In addition, the breakdown induced fluctuations may promote undesirable fluid–structure interactions on aircraft components intersecting the vortex path. Such is the case of tail buffet present in twin-tailed aircraft. Reviews of important aspects of vortex breakdown on delta wings have been provided in [36,39,40]. These indicate that despite recent progress, vortex breakdown still remains a challenge in its fundamental understanding, prediction and control. Further insight into this flow phenomenon could be achieved by systematic experimental and computational studies describing the complex 3D, unsteady structure of vortex breakdown flow fields. The present section describes spurious solutions encountered while performing a detailed computational study in [36–38] of the spiral vortex breakdown structure above a slender delta wing.

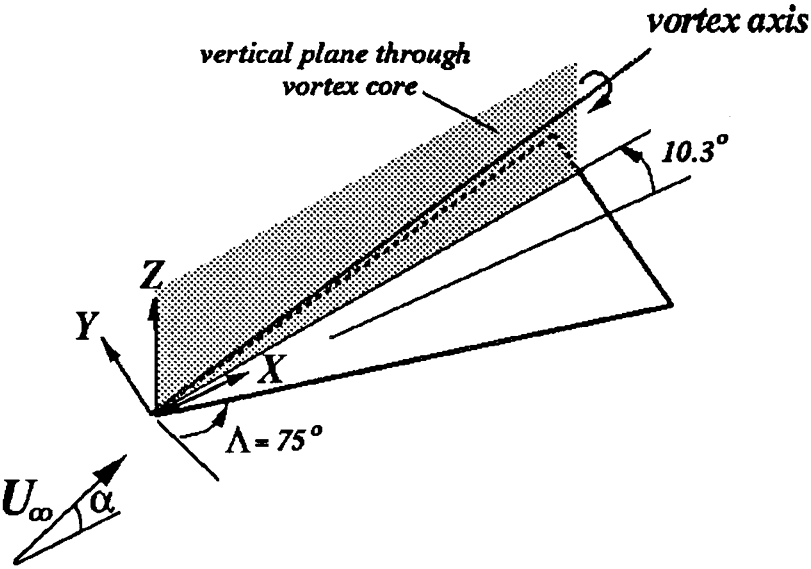

Figure 15. Delta wing configuration.

The flow configuration considered in [36–38] consists of a flat-plate delta wing with a sweep angle of $\Lambda = 75°$ and a free-stream velocity U_∞ depicted in Figure 15. The free-stream Mach number and the Reynolds number based on the centerline chord are 0.2 and 9.2×10^3 respectively. The sweep angle and Reynolds number were selected to permit comparison with the extensive experiments of Magness [41].

The governing equations for the present simulations are the unsteady, 3D compressible full Navier–Stokes equations supplemented by the perfect gas law, Sutherland's viscosity formula and the assumption of a constant Prandtl number ($Pr = 0.72$). These equations are written in strong conservation law form using a general co-ordinate transformation. For the low Reynolds number considered, the flows are assumed to be laminar and no turbulence models are employed.

The governing equations are numerically solved employing the implicit, approximate factorization, Beam–Warming algorithm [42]. The scheme is formulated using backward Euler time differencing and second-order central difference approximations for all spatial derivatives. Fourth-order non-linear dissipation terms are added to control odd–even decoupling. Newton-like subiterations are also incorporated in order to reduce linearization and factorization errors, thereby improving the temporal accuracy and stability properties of the algorithm. A vectorized, time-accurate, 3D Navier–Stokes solver (FDL3DI) has been developed to implement the previous scheme. This code has been validated extensively for both steady and unsteady flow fields (see [38] and references therein).

5.2. Grid structure and boundary conditions

The computational grid topology for the flat-plate delta wing is of the H–H type and is obtained using simple algebraic techniques. For this mesh topology, the boundary conditions are implemented in the following manner. On the lower, upper, lateral and upstream boundaries, characteristic boundary conditions are specified. On the downstream boundary, through which the vortex exits, flow variables are extrapolated from the interior. It should be noted that since the grid is smoothly stretched toward the downstream boundary, the vortical structure has almost entirely dissipated prior to reaching the end of the computational domain. On the wing surface, no-slip, adiabatic conditions are applied in conjunction with the usual zero normal pressure gradient approximation. In this study, only half of the delta wing is considered and symmetry conditions are imposed along the mid-plane of the wing. This is done in order to provide better numerical resolution of the spiral breakdown with a given number of grid points, at the expense of not being able to resolve asymmetric effects. This approach is, therefore, limited to angles of attack for which breakdown location is not too far upstream as to result in changes in breakdown structure due to the interaction of the two vortices.

In order to assess numerical resolution effects, three different grid sizes, denoted as Grid 1, 2 and 3 have been employed with streamwise (X), spanwise (Y), and normal directions (Z) respectively (see Figure 15):

Grid 1: $98 \times 115 \times 102$
Grid 2: $159 \times 107 \times 149$
Grid 3: $209 \times 107 \times 149$

For Grid 1, the streamwise spacing over the wing is $\Delta X/C = 0.02$, where C denotes the wing centerline chord. The spanwise and normal spacing near the vortex axis at the trailing edge ($X/C = 1.0$) are $\Delta Y/C = 0.007$ and $\Delta Z/C = 0.008$ respectively. In Grid 2, the streamwise spacing is halved ($\Delta X/C = 0.01$) in the region where vortex breakdown is anticipated ($0.5 \leq X/C \leq 1.2$). In addition, both the spanwise and normal grid spacings in the vortex axis are reduced by a factor of two. Finally, the finest mesh Grid 3 is obtained from Grid 2 by further decreasing the streamwise spacing in the breakdown region to $\Delta X/C = 0.005$, bringing the cell aspect ratio in the vortex core closer to 1. From a grid resolution study presented in [38], it was concluded that Grid 2 was sufficient to capture the basic structure of a spiral vortex breakdown. The results to be described in the next section pertain to Grids 1 and 2 only.

5.3. *Results*

According to the experiments of Magness [41], vortex breakdown moves upstream over the delta wing when the angle of attack is slowly increased (i.e. in a quasi-static manner) beyond a critical value $\alpha_{cr} \approx 30.7°$. In order to study computationally this quasi-static onset of vortex breakdown, calculations were performed initially near α_{cr} using a 1° increment in angle of attack and employing two of the grids previously described. Although smaller steps in incidence would have been desirable, this was not computationally feasible. The solutions obtained prior to breakdown onset ($\alpha = 30°$) employing an initial angles of attack $\alpha_0 = 29°$ using Grid 1 (Figure 16(a)) and Grid 2 (Figure 16(d)) are found to be in reasonable agreement with each other. The computed onset of vortex breakdown occurred for Grid 1 when α was increased from 31° to 32°, whereas for Grid 2, it took place between 30° and 31°, in closer agreement with experiment [41]. The process by which breakdown appeared in the near-wake and moved over the wing was also found to be qualitatively similar for both grids. Based on these comparisons, one would conclude that the effect of numerical resolution on the quasi-static breakdown onset is small. However, as described below, the non-linear dynamic behavior near α_{cr} was found to be affected significantly by numerical grid resolution when large increments in the initial angle of attack are imposed.

5.3.1. Initial angles of attack. As discussed in [36], some experimental studies have reported the existence of vortex breakdown static hysteresis on delta wings (i.e. multiple, time-asymptotic solutions for a given static angle of attack). Motivated by these findings, the existence of non-unique solutions for different initial conditions was investigated numerically. However, instead of observing static hysteresis phenomena similar to that in some of the experimental studies, spurious behavior due to the numerics was encountered. Computations were performed on Grids 1 and 2 for $\alpha = 30°$ using three different *jump-start* initial angles of attack α_0. With the exception of the initial conditions and grids, all remaining numerical parameters (i.e. time step, damping coefficient, time marching procedure and boundary conditions) were kept the same. In all of the computations, the fixed non-dimensional $\Delta t^+ = 0.0005$. This non-dimensional Δt^+ is equal to the dimensional Δt times U_∞/C. The choice of the fixed Δt is based on the study reported in [38]. The three initial angles of attack α_0 denoted by Cases a, b and c are:

Case a: $\alpha_0 = 29°$
Case b: $\alpha_0 = 25°$
Case c: $\alpha_0 = 17°$

5.3.2. Grid 1. The computed lift coefficient histories obtained on Grid 1 for the above three initial conditions are shown in Figure 17, which exhibit three distinct numerical solutions. The Case a solution corresponds to the columnar (no breakdown) solution shown in Figure 16(a). For Case b, with a mild jump in the initial angle of attack $\alpha_0 = 25°$ to the desired $\alpha = 30°$, the lift coefficient history appears to be time periodic. This solution asymptotes to a flow containing a mild vortex breakdown near the wing trailing edge as shown in Figure 16(b). The

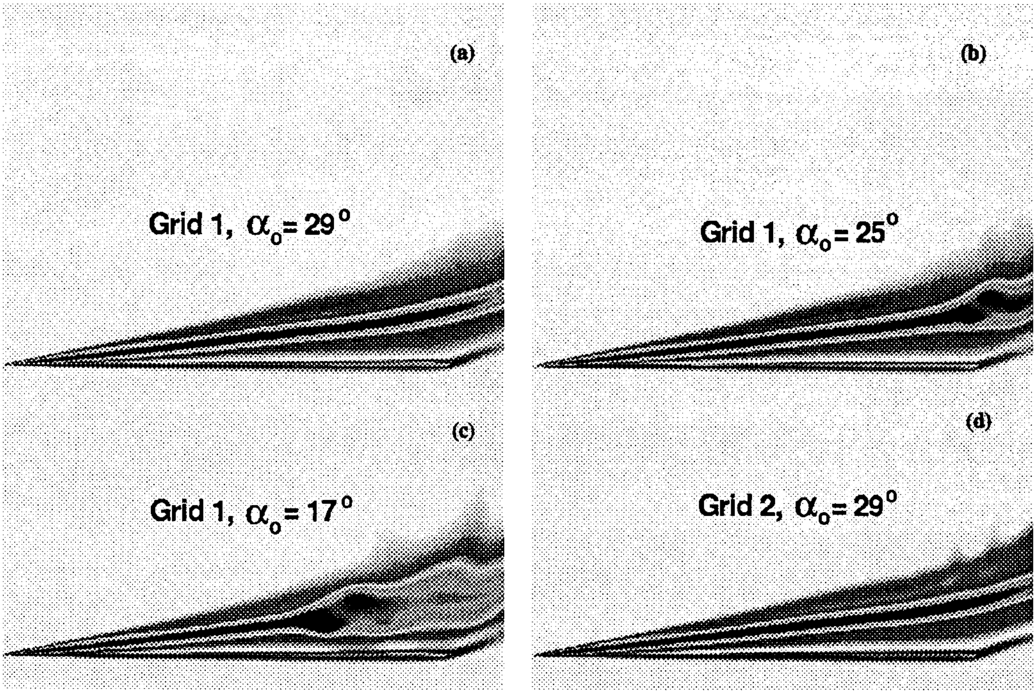

Figure 16. Contours of total pressure on vertical plane through vortex center.

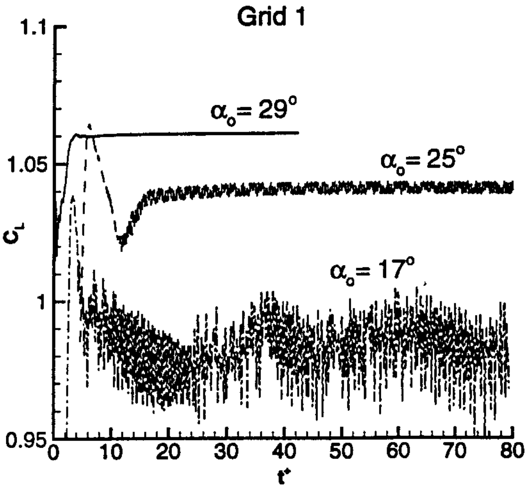

Figure 17. Lift coefficient time histories computed on Grid 1 for $\alpha = 30°$ using three different initial angles of attack.

frequency spectra of the streamwise velocity fluctuations at a point within the reverse flow region in the vortex core is given in Figure 18. It indicates the nearly periodic character of this spiral breakdown. For Case c, a third distinct solution was obtained for a large jump in the initial angle of attack from $\alpha_0 = 17°$ to the desired $\alpha = 30°$. The lift coefficient time history appears to be chaotic-like. This flow field exhibits breakdown well upstream of the trailing edge, as shown in Figure 16(c). Also, the corresponding velocity fluctuations associated with this stronger breakdown display multiple frequencies (Figure 19). Both Cases b and c were run till $t^+ = tU_\infty/C \approx 80$, during which time no tendency was observed for the breakdown to leave the wing. For the purpose of comparison with breakdown computations in tubes or isolated vortices, $t^+ = 80.0$ corresponds in the present case to 2400 characteristic times based on the vortex core radius at $X/C = 0.5$. Comparison of the three solutions in terms of the X component of vorticity in the vortex core at a location upstream of breakdown ($X/C = 0.4$) is

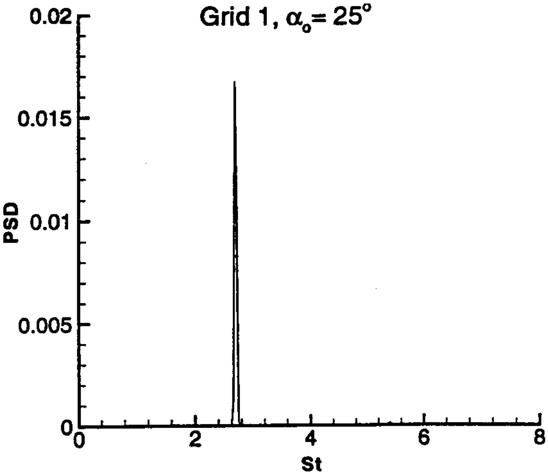

Figure 18. Frequency spectra of velocity fluctuations at point within vortex breakdown region for $\alpha_0 = 25°$.

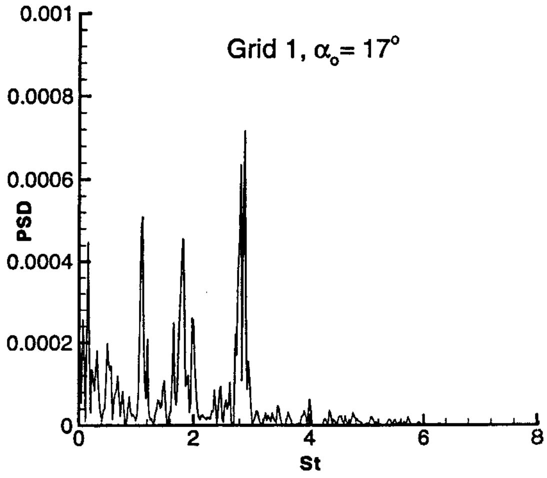

Figure 19. Frequency spectra of velocity fluctuations at point within vortex breakdown region for $\alpha_0 = 17°$.

shown in Figure 20. All flow solutions are seen to be essentially the same at this upstream location, indicating that the different cases are not simply due to lags in the development of the vortex following a change in angle of attack.

5.3.3. Grid 2. In order to investigate the validity of the qualitative behavior displayed by the finite difference solutions computed on Grid 1, calculations were also performed on Grid 2 for $\alpha = 30°$ using the same three initial conditions. The corresponding lift coefficient histories are shown in Figure 21. Instead of obtaining three distinct solutions as in the Grid 1 case, the lift coefficient time histories for the three initial data using Grid 2 evolved to a similar behavior at a later stage of the time integration. The flow structure of Case a is given in Figure 16(d). On this finer mesh, the solution exhibits unsteady boundary layer separation near the wing trailing edge, which results in the observed lift coefficient fluctuations. Notice, however, that the mean C_L is in close agreement with the corresponding value on Grid 1 (Figure 17,

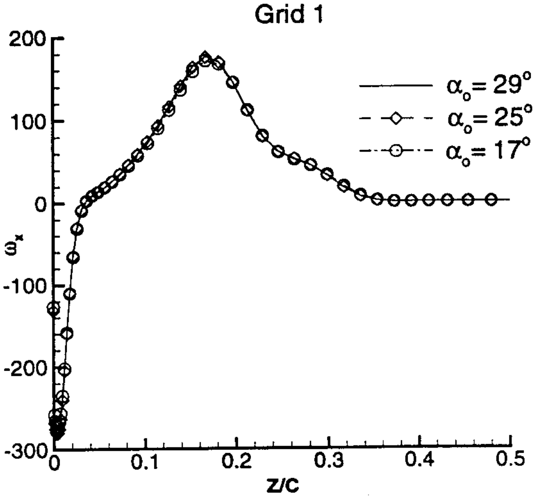

Figure 20. Axial vorticity profile through the vortex core upstream of breakdown for the three initial angles of attack.

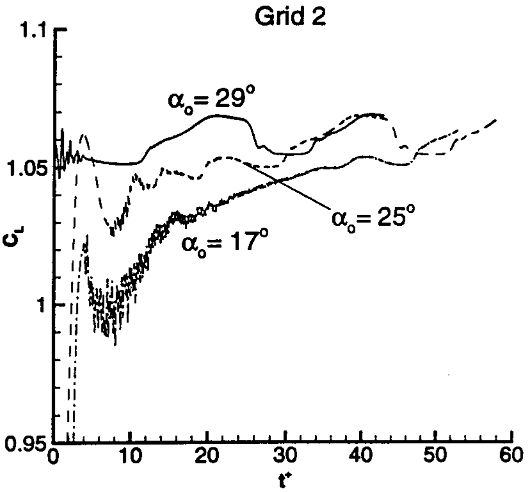

Figure 21. Lift coefficient time histories computed on Grid 2 for $\alpha = 30°$ using three different initial angles of attack.

$\alpha_0 = 29°$). This unsteady phenomenon, captured with the improved spatial resolution, is entirely separate from vortex breakdown and does not significantly affect the vortex core (as seen by comparison of Figure 16(a) and (d)). For Case b, vortex breakdown appears transiently above the wing and penetrates upstream up to $X/C \approx 0.85$, as described in [37]. However, later on, breakdown moves downstream off the wing and into the wake, albeit at a very slow rate. By $t^+ \approx 30.0$, the computed lift coefficient for Case b has reached the same level and characteristic behavior found for Case a, and the flow structure (not shown) is essentially the same as that of Figure 16(d). For Case c, a strong vortex breakdown is induced upstream of $X/C = 0.8$ (see [37]). As before, it proceeds downstream at a very low speed, eventually leaving the wing. The computed lift coefficient (Figure 21) is again observed to increase toward the same level attained in Cases a and b. Examination of the flow fields above the wing for Cases a, b and c in Grid 2 indicated that they all asymptote to the same columnar solution.

The previous results clearly indicate the different dynamic qualitative behavior displayed by the discrete equations on the two grids employed. With the coarser mesh, non-unique solutions that exhibit vortex breakdown are achieved for $\alpha < \alpha_{cr}$ if a sufficiently large $\Delta\alpha$ is imposed in the initial conditions. When the finer grid is utilized, however, the non-unique solutions are no longer found. Vortex breakdown is still induced transiently above the wing but it eventually moves into the wake, albeit at very low speed. The behavior computed on Grid 2 is in agreement with the experiments of Magness [41]. In these experiments it is found that when the wing is pitched at a high rate from $\alpha = 5°$ to $\alpha = 30°$ (below α_{cr}), breakdown occurs over the wing up to $X/C \approx 0.6$. Upon cessation of the motion, however, breakdown leaves the wing, and no static hysteresis (due to multiple solutions) was found.

5.4. Implications of spurious behavior

The above discrepancies in qualitative behavior obtained with the two levels of spatial resolution indicate either that (1) spurious time asymptotic solutions containing breakdown can be obtained on underresolved grids, or that (2) the basins of attractions (allowable initial data) of the various solutions (if they exist) change vastly with mesh spacing as observed in simple model problems [9,16] and in Sections 2 and 3. Regardless of the cause, it can be safely concluded that for the given model problem and flow field conditions, the non-unique solutions exhibited by Grid 1 are numerical artifacts. Although a precise explanation cannot be offered at present, the first possibility is postulated as being the reason for these discrepancies. It is possible that the larger mesh spacing in Grid 1 provides an artificial mechanism for wave-trapping if breakdown is transiently induced. However, further work is clearly required to verify this hypothesis. In the meantime, these results serve to point out the danger associated with interpreting complex flow behavior computed with underresolved meshes. Since Grid 1 is actually finer than grids commonly used in full aircraft simulations, the present results have important implications for practical CFD studies where systematic resolution assessments are not always feasible. The spurious dynamic behavior discussed is particularly relevant, since high angle of attack calculations are typically started (in order to minimize computer time) with abrupt uniform flow initial conditions or with discrete jumps in angle of attack that may induce transient vortex breakdown.

6. CONCLUDING REMARKS

Refinement studies were performed on four CFD computations to illustrate spurious behavior in underresolved grids and/or semi-implicit temporal discretizations. These examples were chosen based on their non-apparent spurious behaviors that were difficult to detect without extensive grid and/or temporal refinement studies and without some knowledge from dynamical systems theory. Using knowledge from dynamical systems theory, various types of spurious behaviors that are numerical artifacts were systematically identified. Each example illustrates different spurious behaviors as discussed in Sections 2–5.

Among the examples, an analysis similar to that in References [2–4] is possible only for the 1D chemically relaxed non-equilibrium flow model. The allowable upstream initial inputs that are devoid of spurious solution as a function of the grid spacing are completely mapped out for the studied scheme. The results illustrate the sensitivity of the allowable initial input to slight increases in the grid spacing. For the fluid–structure interaction model, studies showed that spurious behaviors exhibited by the semi-implicit approach can be eliminated using a reduced time step or a fully implicit coupling approach. Without a comprehensive time step refinement study, it is difficult to determine if the numerical solution is representative of the true physics of the problem.

Among the four examples, the DNS study of the backward-facing step was by far the most controversial concerning the transition point Reynolds number (in the early 1990s). As illustrated, long-time transients and numerically induced chaotic transients exhibited in large scale DNS or other time accurate computations are not easy to detect due to the CPU intensive nature of the simulations. The study also revealed a non-standard guideline in grid clustering and grid adaptation. Fine grids are needed in regions of smooth flows in order to avoid spurious solutions. The fine grid requirement of the smooth solution is contrary to the standard logic in grid clustering and grid adaptation methods.

In the case of the 3D vortex breakdown on delta wings, there already exist uncertainties in experimental studies by different investigators on multiple time asymptotic solutions for a given static angle of attack. The spurious behaviors observed in numerical simulations contribute to additional uncertainties if systematic resolution assessments are not performed.

In all of the underresolved grid cases, the grids actually are finer than grids commonly used in realistic complex CFD simulations. The three semi-implicit methods considered are typical numerical procedures employed in active research areas, such as chemically reacting flows, combustion, fluid–structure interactions, DNS and large eddy simulations (LES). The present study serves to point out the various possible dangers of misinterpreting numerical simulations of realistic complex flows that are constrained by available computing power. In large scale computations where the physics of the problem under study is not well-understood and numerical simulations are the only viable solutions, a knowledge of the global non-linear behavior of numerical algorithms can aid in the identification of the sources of numerical uncertainties in CFD.

The observed spurious behavior related to underresolved grid cases is particularly relevant to DNS and LES. Spatial resolutions in DNS and LES are largely dictated by the computer power, especially when numerical algorithms other than high accuracy spectral methods are employed. LES, by design, filters out the small scales from the non-linear Navier–Stokes equations. The effect of small scales on the large scale motion is accounted for by the subgrid scale model. Spurious behaviors due to underresolved grids in LES can play a major but different role from DNS. A dynamical approach study on the effect of underresolved grids is postulated to be useful in pinpointing the limitation of DNS and LES approaches and their associated spurious behaviors that might be otherwise difficult to detect. These are subjects of future investigations.

ACKNOWLEDGMENTS

The authors wish to thank Philip M. Gresho for initiating the collaboration between the first two authors and for the many helpful discussions throughout the course of this work. The strong encouragement of William L. Oberkampf and Daniel P. Aeschliman on this line of research is gratefully acknowledged. Special thanks to Thomas J. Coakley, David K. Gartling, Terry L. Holst, Laurence R. Keefe, William L. Oberkampf and Marcel Vinokur for their critical review of the manuscript. The work of J.R. Torczynski was performed at Sandia National Laboratories. Sandia is a multiprogram laboratory operated by the Sandia Corporation, a Lockheed Martin Company, for the US Department of Energy under Contract DE-ACO4-94AL85000. The work of S.A. Morton and M.R. Visbal was sponsored by the Air Force Office of Scientific Research under Task 2307 AW, monitored by Len Sakell, and supported in part by a grant of HPC time from the DoD HPC Shared Resource Center ASC at Wright-Patterson AFB, OH.

REFERENCES

1. H.C. Yee, P.K. Sweby and D.F. Griffiths, 'Dynamical approach study of spurious steady state numerical solutions for non-linear differential equations, part I: The dynamics of time discretizations and its implications for algorithm development in computational fluid dynamics', *NASA TM-102820*, April 1990; *J. Comput. Phys.*, **97**, 249–310 (1991).
2. H.C. Yee and P.K. Sweby, 'Global asymptotic behavior of iterative implicit schemes', *RIACS Tech. Report 93.11*, NASA Ames Research Center, December, 1993; *Int. J. Bifurcation Chaos*, **4**, 1579–1611 (1994).
3. H.C. Yee and P.K. Sweby, 'Dynamical approach study of spurious steady state numerical solutions for non-linear differential equations, part II: Global asymptotic behavior of time discretizations', *RNR-92-008*, NASA Ames Research Center; *Int. J. Comput. Fluid Dyn.*, **4**, 219–283 (1995).
4. H.C. Yee and P.K. Sweby, 'On superstable implicit methods and time marching approaches', *RIACS Technical Report 95.12*, NASA Ames Research Center, July 1995; *Proc. Conf. on Numerical Methods for Euler and Navier–Stokes Equations*, University of Montreal, Canada, September 14–16, 1995; *Int. J. Comput. Fluid Dyn.*, **8**, 265–286 (1997).
5. A. Lafon and H.C. Yee, 'Dynamical approach study of spurious steady state numerical solutions for non-linear differential equations, part III: The effects of non-linear source terms in reaction–convection equations', *NASA Tech. Memo. 103877*; *Comput. Fluid Dyn.*, **6**, 1–36 (1996).

6. A. Lafon and H.C. Yee, 'Dynamical approach study of spurious steady state numerical solutions of non-linear differential equations, part IV: Stability vs. numerical treatment of non-linear source terms', *ONERA-CERT Tech. Report DERAT 45/5005.38*; *Comp. Fluid Dyn.*, **6**, 89–123 (1996).
7. D.F. Griffiths, P.K. Sweby and H.C. Yee, 'On spurious asymptotic numerical solutions of explicit Runge–Kutta schemes', *IMA J. Numer. Anal.*, **12**, 319–338 (1992).
8. D.F. Griffiths, A.M. Stuart and H.C. Yee, 'Numerical wave propagation in hyperbolic problems with non-linear source terms', *SIAM J. Numer. Anal.*, **29**, 1244–1260 (1992).
9. H.C. Yee and P.K. Sweby, 'Non-linear dynamics and numerical uncertainties in CFD', *NASA TM-110398*, April 1996.
10. M.A. Aves, D.F. Griffiths and D.J. Higham, 'Does error control suppress spuriosity?', *SIAM J. Numer. Anal.*, **34**, 756–778 (1997).
11. P.M. Gresho, *Incompressible Flow and the Finite Element Method*, Wiley, Chichester, 1998.
12. D. Estep and R. William, 'The structure of an adaptive differential equation solver', *Math. Models Methods Appl. Sci.*, **6**, 535–568 (1996).
13. C. Johnson, 'On computability and error control in CFD', *Inter. J. Numer. Methods Fluids*, **20**, 777–788 (1995).
14. C. Johnson, R. Rannacher and M. Boman, 'Numerics and hydrodynamics stability: toward error control in computational fluid dynamics', *SIAM J. Numer. Anal.*, **32**, 1058–1079 (1995).
15. P.K. Sweby and H.C. Yee, 'On the dynamics of some grid adaptation schemes', *Proc. 4th Int. Conf. on Numerical Grid Generation in CFD and Related Fields*, University College of Swansea, UK; *RIACS Technical Report 94.02*, February, 1994.
16. H.C. Yee and P.K. Sweby, 'Some aspects of numerical uncertainties in time marching to steady state computations', *AIAA-96-2052*, *27th AIAA Fluid Dynamics Conference*, New Orleans, LA, June 18–20, 1996; *AIAA J.*, **36**, 712–724 (1998).
17. P.K. Sweby, A. Lafon and H.C. Yee, 'On the dynamics of computing a chemically relaxed non-equilibrium flow', *ICFD Conference on Numerical Methods for Fluid Dynamics*, Oxford, UK, April 3–6, 1995.
18. C. Park, 'On convergence of chemically reacting flows', *AIAA-85-0247*, *ALAA 23rd Aerospace Sciences Meeting*, Reno, NV, January 14–17, 1985.
19. Workshop on Hypersonics, *Proc. Workshop on Hypersonic Flows for Reentry Problems*, *Part II*, Antibes, France, 15–19 April, 1991.
20. V. Mulard and G. Moules, 'Non-equilibrium viscous flow calculations in hypersonic nozzles', *Proc. of the Workshop on Hypersonic Flows for Reentry Problems*, *Part II*, Antibes, France, 15–19 April, 1991.
21. L. Keefe, Private communication, unpublished data, 1996.
22. C. Grebogi, E. Ott and J.A. Yorke, 'Crises, sudden changes in chaotic attractors, and transient chaos', *Physica D*, **7** 181–200 (1983).
23. H.C. Yee, R.D. Henderson and M. Poliashenko, 'On the numerical prediction of flow transition', *10th Int. Conf. for Finite Elements in Fluid*, Tucson, AZ, January 5–8, 1998.
24. P.M. Gresho, D.K. Gartling, J.R. Torczynski, K.A. Cliffe, K.H. Winters, T.J. Garratt, A. Spence and J.W. Goodrich, 'Is the steady viscous incompressible two-dimensional flow over a backward-facing step at $Re = 800$ stable?', *Int. J. Numer. Methods Fluids*, **17**, 501–541 (1993).
25. L. Kaiktsis, G.E. Karniadakis and S.A. Orszag, 'Onset of three-dimensionality, equilibria, and early transition in flow over a backward-facing step', *J. Fluid Mech.*, **231**, 501–528 (1991).
26. J.R. Torczynski, 'A grid refinement study of two-dimensional transient flow over a backward-facing step using a spectral element method', in J.C. Dutton and L.P. Purtell (eds.), *Separated Flows*, FED Vol. 149, ASME, New York, 1993.
27. L. Kaiktsis, G.E. Karniadakis and S.A. Orszag, 'Unsteadiness and convective instabilities in two-dimensional flow over a backward-facing step', *J. Fluid Mech.*, **321**, 157–187 (1996).
28. A. Fortin, M. Jardak, J.J. Gervais and R. Pierre, 'Localization of Hopf bifurcations in fluid flow problems', *Int. J. Numer. Meth. Fluids*, **24**, 1185–1210 (1997).
29. NEKTON, *User's Guide*, *Version 2.8*, Nektonics Inc., Cambridge, MA, 1991.
30. M.J. Smith, *Flight Loads Prediction Methods for Aircraft: Vol I. Euler/Navier–Stokes Aeroelastic Method (ENS3DAE) Technical Development Summary: Version 4.0*, D.M. Schuster, J. Vadyak and E.H. Alta, supersedes WRDC-TR-89-3104, November 1989.
31. G.P. Guruswamy, 'Unsteady aerodynamic and aeroelastic calculations for wings using Euler equations', *AIAA J.*, **28**, 461–469 (1990).
32. S.A. Morton and P.S. Beran, 'Non-linear analysis of airfoil flutter at transonic speeds', *AIAA-95-1905*, *AIAA 13th AIAA Applied Aerodynamics Conference*, San Diego, CA, June 19–22, 1995.
33. J. Alonso, L. Martinelli and A. Jameson, 'Multigrid unsteady Navier–Stokes calculations with aeroelastic applications', *AIAA Paper-95-0048*, January 1995.
34. H.M. Blackburn and G.E. Karniadakis, 'Two- and three-dimensional vortex-induced vibration of a circular cylinder', *ISOPE-93 Conference*, Singapore, 1993.
35. S.A. Morton, R.B. Melville and M.R. Visbal, 'Accuracy and coupling issues of aeroelastic Navier–Stokes solutions on deforming meshes', *AIAA Paper-97-1085*, April 1997.
36. M.R. Visbal, 'Computational and physical aspects of vortex breakdown on delta wings', *AIAA-95-0585*, January 1995.

37. M.R. Visbal, 'Numerical simulation of spiral vortex breakdown above a delta wing', *AIAA-95-2309*, June 1995.
38. M.R. Visbal, 'Computed unsteady structure of spiral vortex breakdown on delta wings', *AIAA-96-2074*, June 1996.
39. M. Lee and C.-M. Ho, 'Lift force on delta wings', *Appl. Mech. Rev.*, **43**, 209–221 (1990).
40. D. Rockwell, 'Three-dimensional flow structure on delta wings at high angle of attack: experimental concepts and issues', *AIAA-93-0550*, January 1993.
41. C. Magness, 'Unsteady response of the leading edge vortices on a pitching delta wing', *Ph.D. Dissertation*, Lehigh University, May 1991.
42. R.M. Beam and R.F. Warming, 'An implicit factored scheme for the compressible Navier–Stokes equations', *AIAA J.*, **16**, 393–402 (1978).